

PENNSTATE



Enhancement of Corrosion Resistance and Mechanical Properties of Light-Weight Metals Through the Use of Graded Nonequilibrium Microstructures - Second Annual Report

Prepared and Submitted by:

Barbara Shaw
Kelly Kennedy
Kirk Scammon
Ed Principe

Department of Engineering Science and Mechanics
The Pennsylvania State University

Submitted to:
Office of Naval Research
800 North Quincy Street
Arlington, VA 22217-5000

December 1995

DTIC QUALITY INSPECTED 4

19960208 052

DISTRIBUTION STATEMENT A

Approved for public release;
Distribution Unlimited

REPORT DOCUMENTATION PAGE

Form Approved
OMB No. 0704-0188

1a. REPORT SECURITY CLASSIFICATION Unclassified			1b. RESTRICTIVE MARKINGS None	
2a. SECURITY CLASSIFICATION AUTHORITY			3. DISTRIBUTION/AVAILABILITY OF REPORT Unrestricted	
2b. DECLASSIFICATION/DOWNGRADING SCHEDULE				
4. PERFORMING ORGANIZATION REPORT NUMBER(S)			5. MONITORING ORGANIZATION REPORT NUMBER(S)	
6a. NAME OF PERFORMING ORGANIZATION Penn State University	6b. OFFICE SYMBOL (if applicable)	7a. NAME OF MONITORING ORGANIZATION		
6c. ADDRESS (City, State, and ZIP Code) Dept. of Engineering Science and Mechanics 227 Hammond Bldg. University Park, PA 16802		7b. ADDRESS (City, State, and ZIP Code)		
8a. NAME OF FUNDING/SPONSORING ORGANIZATION Office of Naval Research	8b. OFFICE SYMBOL (if applicable) Code 3312	9. PROCUREMENT INSTRUMENT IDENTIFICATION NUMBER		
8c. ADDRESS (City, State, and ZIP Code) 800 North Quincy St. Arlington, VA 22217-5000		10. SOURCE OF FUNDING NUMBERS		
		PROGRAM ELEMENT NO.	PROJECT NO. N00014-93-1-0537	TASK NO.
				WORK UNIT ACCESSION NO.
11. TITLE (Include Security Classification) Enhancement of Corrosion Resistance and Mechanical Properties of Light-Weight Metals Through the Use of Graded Nonequilibrium Microstructures				
12. PERSONAL AUTHOR(S) Barbara Shaw, Kelly Kennedy, Kirk Scammon and Ed Principe				
13a. TYPE OF REPORT Technical	13b. TIME COVERED FROM 11/1/94 TO 12/1/95	14. DATE OF REPORT (Year, Month, Day) 95/12/22	15. PAGE COUNT 58	
16. SUPPLEMENTARY NOTATION				
17. COSATI CODES			18. SUBJECT TERMS (Continue on reverse if necessary and identify by block number)	
FIELD	GROUP	SUB-GROUP	Functionally graded materials, nonequilibrium alloying, corrosion resistant Al Alloys, corrosion resistant Mg alloys	
19. ABSTRACT (Continue on reverse if necessary and identify by block number) Designs for the future will place extreme demands on light-weight materials. In order to meet these future challenges, it is vital that an emphasis be placed on tailor-making materials with enhanced specific properties. Through the use of rapid solidification processing, advances have been made in our ability to engineer materials--but we have yet to be able to tailor-make a light-weight alloy with all of the characteristics we desire. A new approach to tailor-making alloys with the enhanced properties we desire is to use nonequilibrium alloying techniques such as sputter or electron-beam (e-beam) evaporation to grade the structure and composition of an alloy during processing. Such alloys could be designed to take advantage of recent advances in enhancing both the mechanical properties and the corrosion resistance of Al and Mg. For conventional Al alloys, a combination of high-strength and superior (localized) corrosion resistance are mutually exclusive. In order to achieve high strengths, precipitates are necessary in the microstructure. On the other hand, in order to exhibit superior corrosion performance, a one phase structure is usually required (precipitates can establish microgalvanic cells which lead to accelerated corrosion of (continued on back)				
20. DISTRIBUTION/AVAILABILITY OF ABSTRACT <input checked="" type="checkbox"/> UNCLASSIFIED/UNLIMITED <input type="checkbox"/> SAME AS RPT. <input type="checkbox"/> DTIC USERS			21. ABSTRACT SECURITY CLASSIFICATION	
22a. NAME OF RESPONSIBLE INDIVIDUAL B.A. Shaw			22b. TELEPHONE (Include Area Code) (814) 865-7828	22c. OFFICE SYMBOL

19 Abstract (continued)

the precipitate or the alloy adjacent to the precipitate). However, both high-strength and superior corrosion resistance could be combined in one material if the structure and composition of the alloy were graded during nonequilibrium processing.

Work during the second year of this investigation focused the production of e-beam evaporated (nonequilibrium) Al-Mo alloys at Idaho National Engineering Lab, the fabrication of an e-beam evaporation system at Penn State, and an investigation of the influence of deposit morphology on alloy corrosion performance. Results obtained within the last year have shown that it is possible to produce e-beam evaporated Al-Mo alloys which have significantly enhanced localized corrosion resistance. For example, an Al-7 volume percent Mo alloy exhibited a breakdown (pitting) potential that was 600 mV higher than that of 6061 Al. As a result of the higher deposition temperatures for the e-beam evaporation process, precipitates were noted in the e-beam evaporated alloys when deposition temperatures were in excess of 300 C. Fortunately, the presence of these precipitates did not severely alter the range of passivity for the alloys (as measured in an anodic polarization scan); instead, the precipitates increased the passive current densities of the alloys by about one order of magnitude. Preliminary cross-section analysis of the e-beam evaporated materials has revealed that the initial 25 to 50% of the deposit (5 to 10 microns) was very dense, whereas, the top 50 to 75% of the deposit was very columnar in structure with open regions between the columns.

Research on both the sputter and e-beam evaporated materials has clearly shown that defects and deposit morphology (e.g., a columnar structure) play a significant role in pit initiation (breakdown) on these materials. Morphological changes were apparent in the compositionally graded sputter-deposited materials and the degraded performance of these alloys, when compared to the constant solute concentration alloys, was attributed to pit initiation in low solute concentration regions of the deposit (regions at the bottom of deep grooves in the columnar structure). Clearly, full optimization of deposit corrosion resistance will hinge on the production of smooth, dense deposits which do not exhibit a columnar structure. The superior corrosion resistance of the nonequilibrium sputter and e-beam evaporated alloys, despite their less than optimal morphologies, was believed to be the result of enhanced repassivation of the alloys caused by solute enrichment at pit initiation sites.

PENNSTATE



Department of Engineering Science
and Mechanics

(814) 865-4523
Fax: (814) 863-7967
<http://www.esm.psu.edu>

The Pennsylvania State University
227 Hammond Building
University Park, PA 16802-1401

January 31, 1996

Defense Technical Information Center
Building 5, Cameron Station
Alexandria, VA 22304-6145

Dear Sir/Madam:

In accordance with the reporting requirements of contract N00014-93-1-0537, enclosed herewith are two copies of our Second Annual Report entitled, "Enhancement of Corrosion Resistance and Mechanical Properties of Light-Weight Metals Through the Use of Graded Nonequilibrium Microstructures".

Sincerely,

A handwritten signature in cursive script that reads "Barbara A. Shaw".

Barbara A. Shaw
Associate Professor of Engineering
Science and Mechanics

BAS/car

Enclosures

PENNSTATE



Enhancement of Corrosion Resistance and Mechanical Properties of Light-Weight Metals Through the Use of Graded Nonequilibrium Microstructures - Second Annual Report

Prepared and Submitted by:

Barbara Shaw
Kelly Kennedy
Kirk Scammon
Ed Principe

Department of Engineering Science and Mechanics
The Pennsylvania State University

Submitted to:
Office of Naval Research
800 North Quincy Street
Arlington, VA 22217-5000

December 1995

TABLE OF CONTENTS

Abstract	i
Introduction.	1
Background	2
Experimental Procedures	12
Results and Discussion	16
Summary.	54
References	54

Abstract

Designs for the future will place extreme demands on light-weight materials. In order to meet these future challenges, it is vital that an emphasis be placed on tailor-making materials with enhanced specific properties. Through the use of rapid solidification processing, advances have been made in our ability to engineer materials -- but we have yet to be able to tailor-make a light-weight alloy with all of the characteristics we desire. A new approach to tailor-making alloys with the enhanced properties we desire is to use nonequilibrium alloying techniques such as sputter or electron-beam (e-beam) evaporation to grade the structure and composition of an alloy during processing. Such alloys could be designed to take advantage of recent advances in enhancing both the mechanical properties and the corrosion resistance of Al and Mg. For conventional Al alloys, a combination of high-strength and superior (localized) corrosion resistance are mutually exclusive. In order to achieve high strengths, precipitates are necessary in the microstructure. On the other hand, in order to exhibit superior corrosion performance, a one phase structure is usually required (precipitates can establish microgalvanic cells which lead to accelerated corrosion of the precipitate or the alloy adjacent to the precipitate). However, both high-strength and superior corrosion resistance could be combined in one material if the structure and composition of the alloy were graded during nonequilibrium processing.

Work during the second year of this investigation focused the production of e-beam evaporated (nonequilibrium) Al-Mo alloys at Idaho National Engineering Lab, the fabrication of an electron-beam (e-beam) evaporation system at Penn State, and an investigation of the influence of deposit morphology on alloy corrosion performance. Results obtained within the last year have shown that it is possible to produce e-beam evaporated Al-Mo Alloys which have significantly enhanced localized corrosion resistance. For example, an Al -7 volume percent Mo alloy exhibited a breakdown (pitting) potential that was 600 mV higher than that of 6061 Al. As a result of the higher deposition temperatures for the e-beam evaporation process, precipitates were noted in the e-beam evaporated alloys when deposition temperatures were in excess of 300 C. Fortunately, the presence of these precipitates did not severely alter the range of passivity for the alloys (as measured in an anodic polarization scan); instead, the precipitates increased the passive current densities of the alloys by about one order of magnitude. Preliminary cross-sectional analysis of the e-beam evaporated materials has revealed that the initial 25 to 50 % of the deposit (5 to 10 microns) was very dense, whereas, the top 50 to 75 % of the deposit was very columnar in structure with open regions between the columns.

Research on both the sputter and e-beam evaporated materials has clearly shown that defects and deposit morphology (e.g., a columnar structure) play a significant role in pit initiation (breakdown) on these materials. Morphological changes were apparent in the compositionally graded sputter-deposited materials and the degraded performance of these alloys, when compared to the constant solute concentration alloys, was attributed to pit initiation in low solute concentration regions of the deposit (regions at the bottom of deep grooves in the columnar structure). Clearly, full optimization of deposit corrosion resistance will hinge on the production of smooth, dense deposits which do not exhibit a columnar structure. The superior corrosion resistance of the nonequilibrium sputter and e-beam evaporated alloys, despite their less than optimal morphologies, was believed to be the result of enhanced repassivation of the alloys caused by solute enrichment at pit initiation sites.

INTRODUCTION

With each passing year, increasingly more stringent demands are being placed on light-weight materials to implement modern engineering designs. Meeting the requirements of these advanced designs will involve tailor making materials with the specific properties to satisfy application requirements. A new approach to engineering materials which will meet the demands of future designs is to alter the structure and properties of the material as a function of section thickness during processing. Spatial control of materials' properties is not a new concept - surface hardening treatments and coatings have been used for many years to alter a material's surface properties. By gradually transitioning from one material to another, stress concentrations can be reduced and material properties can be spatially optimized. Interest in functionally graded materials (FGMs) has been steadily increasing for the past 10 years and, at present, the most common processing routes include: diffusion processes, spray deposition, liquid or vapor infiltration, and powder processing. This research focuses on a less commonly used method, physical vapor deposition, for producing graded Al and Mg alloys. The vapor deposition route not only provides a convenient means for producing graded materials, it also allows us to circumvent equilibrium solubility limits associated with the more common processing routes and; thus, produce alloys with significantly enhanced corrosion resistance.

Previous ONR-sponsored research [1-10] has shown that the localized corrosion resistance of aluminum can be dramatically enhanced through nonequilibrium alloying with elements such as W, Mo, and Ta. In order to attain the best possible corrosion resistance it is necessary for the transition metal solute to remain in solid solution with the aluminum; in other words, it is necessary to have a one-phase alloy. If present, the second phase particles can act as nucleation sites for pitting corrosion of the Al. However in order to produce high-strength Al alloys, precipitation of a second phase is necessary. Grading the structure of nonequilibrium Al-Mo and Al-W alloys presents a unique means for combining both strength and corrosion resistance in the same alloy -- properties which are mutually exclusive in conventional aluminum alloys. By heat-treating a graded nonequilibrium Al-Mo or Al-W alloy in which the outside layers have relatively high solute concentrations (on the order of 10 to 20 atomic percent) and the inside layers have moderate solute concentrations (less than 10 percent and more than 2 to 3 percent) it should be possible to produce an alloy which has a uniform distribution of fine precipitates for strength through most of the section and a surface that is single-phased and amorphous for corrosion resistance. The primary goals of this research are to investigate the structure and properties of functionally graded nonequilibrium Al and Mg alloys in order to gain a better understanding of the effects of solute concentration and precipitates on the corrosion characteristics and mechanical properties of the alloys. An additional objective of the research is to gain experience in producing functionally graded structures -- experience that could be used to tailor-make monolithic and composite materials with enhanced strength, corrosion, and wear-resistance. Research in the past year has concentrated on evaluating the influence of deposit morphology on alloy corrosion resistance. In addition, an e-beam vapor deposition system was designed and built at PSU during the past year. This system will be used to produce functionally graded Al and Mg alloys during the final year of the program.

BACKGROUND

Nonequilibrium processing techniques such as physical vapor deposition (PVD) [1-13], mechanical alloying [14] and rapid solidification [15] allow for the development of novel alloy compositions and microstructures which can lead to enhanced mechanical properties and corrosion resistance. Of these nonequilibrium methods, PVD provides the most flexibility in the range of properties that can be attained for a particular alloy system. In this research, two vapor deposition methods, sputter deposition and electron-beam (e-beam) evaporation, were used to produce Al-W and Al-Mo alloys with enhanced properties. Both e-beam evaporation and sputter deposition produce alloys with unique morphologies which can significantly influence their performance.

Thin-film Microstructures and Structure Zone Models

Microstructural analyses of thin-films (both surface and cross-sectional views) provide an excellent means for characterizing the films and provide the basis for structure zone models (SZMs) which have been used by several investigators to describe the effects of temperature and pressure on deposit morphology and microstructure. Movchan and Demchishin proposed the first SZM to describe the morphology of thick evaporated films as a function of the homologous temperature, T/T_m (where T is the temperature of the substrate during deposition and T_m is the melting temperature of the deposited film) [16]. The work of Movchan and Demchishin was expanded by Thornton and Hoffman who added a gas pressure axis to the existing model [17]. In addition, Thornton's SZM contained a transition zone, zone T, which was not explicitly included in Movchan and Demchishin's model. It should also be noted that Thornton's model was based on sputtered thin-films; whereas, Movchan and Demchishin's model was derived from data on evaporated films. Similarities in structure between evaporated and sputtered films indicate a fundamental and completely general basis for morphological transitions. The processes which govern film morphology can be broadly categorized as: shadowing, surface diffusion (adatom mobility), and bulk diffusion. These processes are inherent in all vapor deposition methods and are controlled through interactions between temperature, chemistry, and bombardment. Competition among the processes dictates which type of structure prevails and under what combinations of conditions a particular structure can exist. A detailed understanding of a specific system requires a fairly intimate knowledge of the controlling variables.

Thornton's SZM is presented in Figure 1 [17]. In this model, zone I is characterized by open boundaries between tapered crystals with domed tops. As a result of the limited surface diffusion when T/T_m is less than 1, atoms impinging on the substrate surface are essentially immobile and shielding by surface atoms leads to the open structure. Growth of these zone 1 deposits is dominated by self-shadowing. Low adatom mobility in this regime of the diagram leads to pinning of atoms and multiple boundaries between groups of atoms which establishes both a micro and a macro structure within the deposit. Roughness of the substrate surface can further influence the macrostructure of the deposit, providing more surface pinning sites. It should be noted that the micro and macro structures can be either crystalline or amorphous. Regardless of the degree of order within a system, low density regions (grain

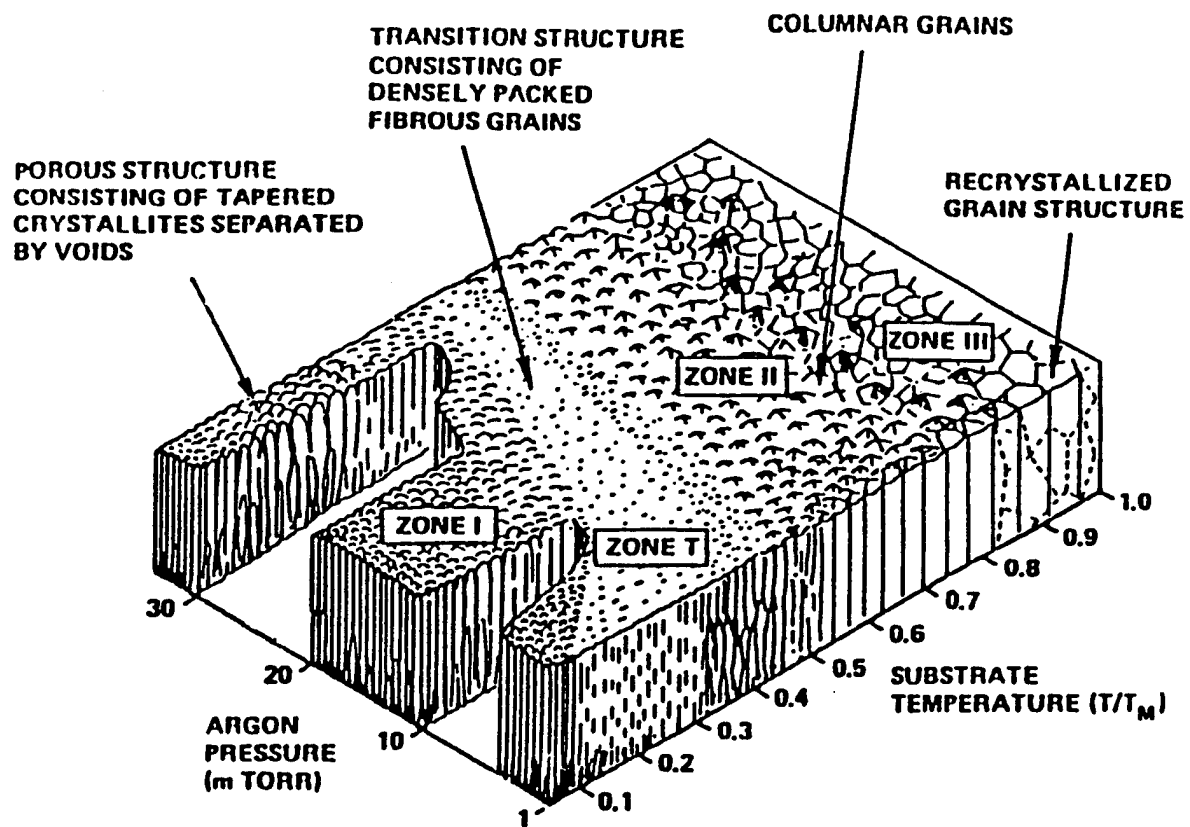


Figure 1. Thornton's structure zone model(SZM) based on working gas pressure and reduced temperature [17].

boundary analogs) will exist due to the inherent nature of film growth in the low adatom mobility regime. Competition as the film thickens causes certain clusters to preferentially dominate, while other clusters die out. At lower substrate temperatures and higher pressures, inert gas adsorption will also act to restrict adatom mobility. Cross-sectional and surface micrographs of a zone 1 SiC film revealing the tapered crystals and domed tops characteristic of this zone are presented in Figure 2.

At a value of T/T_m of approximately 0.1 to 0.3 Thornton described a transition zone identified as zone T. In this range of temperature and pressure surface mobility is increased and atom rearrangement becomes possible. Thus, overshadowing and a more densely packed fibrous array structure result. The smooth, highly reflective surface and dense, fibrous cross-section of a zone T SiC film are depicted in the SEM micrograph shown in Figure 3 [18]. Messier reported that both zone I and zone T morphologies contain "structure within structure" -- a micro-morphology was observed within the macro-morphological columns. This morphology contains a considerable degree of self-similarity which has been associated with fractal geometry [18].

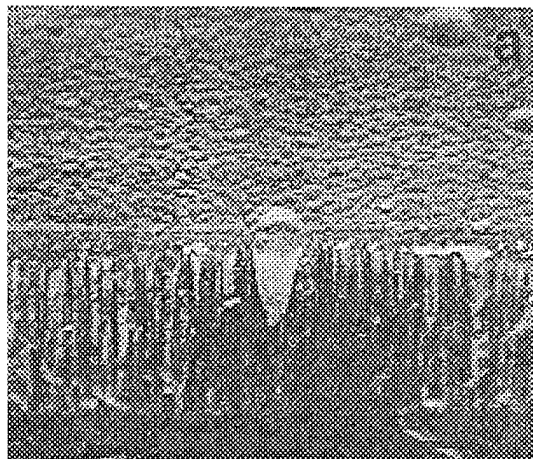
In zone II of Thornton's model, surface diffusion dominates during deposition and a more open columnar structure, compared to zone T, develops. In this region, the openness results from surface faceting and grain growth. In addition, grain boundaries between columns are mobile in the zone. A surface micrograph of a zone II SiC film revealing the intercrystalline boundaries is shown in Figure 4 [19].

When T/T_m is greater than 0.9, a fourth zone (identified as III) is described by Thornton. In this regime, bulk diffusion dominates and if sufficient stress builds up, bulk recrystallization may occur. A near-equilibrium structure is typical and is characterized by flat equiaxed grains. A preferred low energy orientation may develop in this zone.

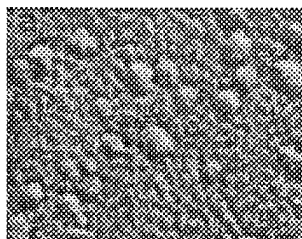
Thornton's SZM was revised by Messier et al. [18] to account for film bombardment, not just from working pressure effects alone but also from the average energy of the deposited sputtered species as it strikes the growing film surface. For example, film bombardment was found to increase when a potential was applied to the substrate. In the case of a potential applied to the substrate, the working gas bombards the growing film during deposition with a force large enough to induce compactness but small enough to prevent resputtering. Messier et al [18] defined a parameter, V_s , the substrate floating potential, which was found to be dependent on both working pressure and the average energy of the bombarding sputtered species. Figure 5 shows Messier's revision of Thornton's SZM based on V_s and the homologous temperature. Messier et al. observed that at low homologous temperatures and low substrate floating potentials, a zone 1 microstructure formed. When V_s was increased and the reduced temperature remained the same, a zone T microstructure prevailed. When the homologous temperature was increased, zone 2 and zone 3 coatings developed.

Microstructure versus Film Thickness

An investigation of microstructure versus film thickness for structures at the zone 1/zone T boundary was conducted by Messier et al. [19,20]. The results of their research concluded that both the morphology and surface roughness intensify with



(a)



(b)

Figure 2. Microstructures of a zone 1 SiC film: (a) cross-sectional view [18], (b) surface view [19].



Figure 3. Cross-sectional microstructure of a zone T SiC film [18].

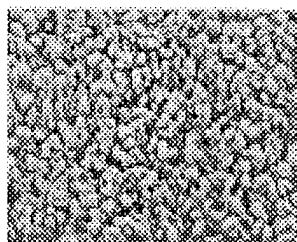


Figure 4. Surface microstructure of a zone II SiC film [19].

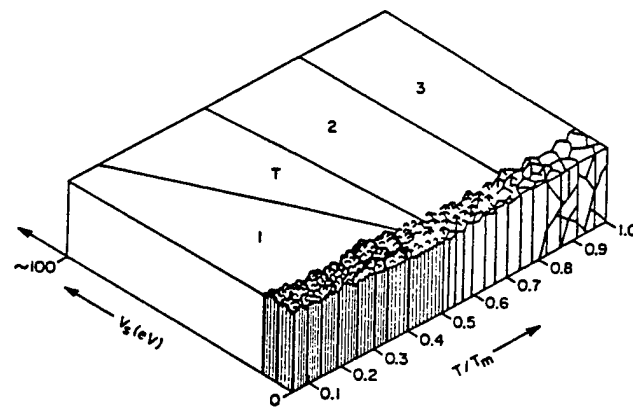


Figure 5. Messier's revised structure zone model showing the microstructural zone regions as a function of substrate floating potential, V_s , and homologous temperature, T/T_m [18].

increasing film thickness [19,20]. Furthermore, these researchers found that the width of the void network increased with increasing film thickness [21]. Note, voids are defined as regions of lower atomic density and a void network is a string of continuous voids surrounding columnar growths. In their study of the growth patterns of amorphous-Si:H films, Messier et al. [22] showed that growth of these films initiated as islands (approx. 50 to 200 Å in diameter) separated by a honeycomb network of voids. Larger islands were found to be composed of "incomplete coalescence of smaller size units". As the film thickness increased, it was noted that the void network formed larger voids in some areas. At film thicknesses of 1200 Å, a super-network consisting of larger voids was discovered surrounding bigger islands of approximately 200 to 400 Å in diameter. Once again, these larger islands were composed of clusters of smaller islands. At the greatest film thickness studied, 10 μm, the large island sizes were found to be 2000 to 5000 Å in diameter. Based on these results, Messier et al. [21] suggested that films defined as zone T may actually be zone 1 microstructures in early developmental stages. Figures 6 a and b illustrate this point. Figure 6a shows a zone 1 microstructure for a thick film, but the cross-sectional cut of this film (part b of the figure) displays early growth and resembles a zone T microstructure. High magnification of the surface of the deposit pictured in Figure 6 a should reveal a pattern of islands separated by a honeycomb void network. As Figure 6 suggests, magnification of the cross-section should show very small gaps in between fine columns. Films with thicknesses of several microns should verify the actual film zone microstructure.

Hillock Growth in Aluminum Alloys

Hillocks are commonly seen in Al thin films under conditions of high compressive stress and are recognized as protrusions of the surface [17,23]. Hillocks have also been observed in oxygen contaminated systems when oxygen pressures ranged from $\approx 2 \times 10^{-5}$ Pa to $\approx 2 \times 10^{-4}$ Pa [24]. In this pressure range, the number of hillocks was found to increase with oxygen pressure. Mechanisms for hillock growth are still under investigation, but studies have suggested that they are caused by nonuniform relaxation of compressive stress causing localized areas to be subjected to greater relaxation [17,23]. These localized areas induce the diffusion of the material from the bulk of the film to the surface. Thus, a hillock pushes out from the base of the film and slides along the grain boundaries, while atoms simultaneously flow to the base of the hillock to fill in the void space -- producing an overall relaxation of the film. Additionally, hillock density was found to be a function of film thickness with thicker films exhibiting more hillocks.

As-Deposited Defects

Defects have been observed on as-deposited films by a variety of scientists [8,22,25-28] and are believed to influence the growth of the deposit and alter its properties. These defects, which include scratches, holes, and protrusions, can result from deposits or defects on the substrate prior to sputtering, scratches which occur during handling of the films, or from high residual stresses in the thin-film causing it to crack or buckle. There may be other reasons for the presence of these defects, but these will not be elaborated on in this section.

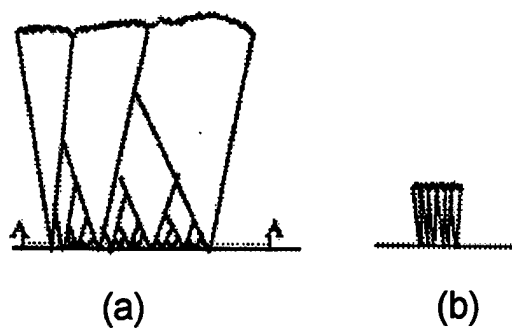


Figure 6. Microstructure dependency on film thickness, showing that thin zone 1 films may appear as zone T films: (a) schematic cross-section of a thick film, and (b) early stage growth of a thick film.

Messier et al. [22] evaluated the influence of substrate scratches on deposit morphology for an amorphous Si-H film. Figure 7 illustrates the results of the study for film thicknesses of 1200 Å, 3000 Å, 1 µm, and 10 µm. This figure reveals that a scratch on the substrate prior to sputtering was translated through the deposit to the surface for the two thinnest films. At film thicknesses of 1 µm, and 10 µm, large cauliflower growths were seen on the deposited film surface at the substrate scratch location. This same study also indicated that film morphology was not affected by the type of substrate. Thus, similar film morphologies were observed for films deposited on KCl and Si substrates.

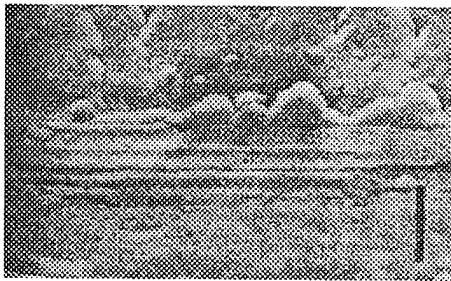
The Effect of Deposit Morphology on Corrosion Resistance

Microstructure versus Corrosion Resistance

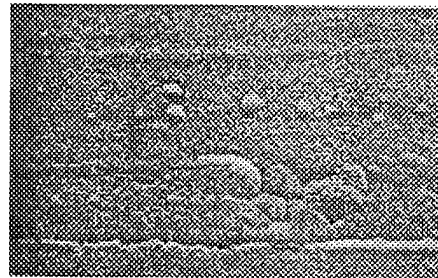
Thakoor et al. [29] investigated the impact of film microstructure on corrosion resistance for an amorphous metal. Their study compared the corrosion resistance of a zone T film with a zone 1 film by depositing a metal with identical parameters at two different working pressures. The zone T film was characterized as smooth and dense with virtually no cross-sectional or topographical features; whereas, the zone 1 film, deposited at a higher working pressure, showed dense, distinctly vertical columnar structures in the cross-section and a rougher surface morphology. These investigators found the zone T alloy to be significantly more corrosion resistant than the zone 1 film. The zone 1 coating showed almost instantaneous dissolution when immersed in an aqueous acidic solution, suggesting that the deep void regions between the columns may have provided a less corrosion resistant surface area for chemical attack. In contrast to this behavior, the zone T alloys (with featureless surfaces) did not dissolve instantaneously. A uniform continuous oxide acting as a barrier to anodic dissolution was believed to be responsible for the enhanced resistance of the zone T deposit.

The study conducted by Thakoor et al. [29] also analyzed the corrosion resistance of oxygen and nitrogen induced microstructures. The oxygen-containing microstructure was prepared with a working gas mixture of $\approx 5 \mu\text{m}$ of Ar and $\approx 2 \mu\text{m}$ of O_2 . As expected, the microstructure was a porous, highly developed zone 1 film. The cross-section of this oxygen-containing film exhibited poorly bonded columns with large voids, and the surface was much rougher than that of the zone 1 film fabricated in pure Ar which was described above. Corrosion tests in aqueous acidic solutions showed that the oxygen-containing film performed in a manner similar to the zone 1 film fabricated in pure Ar. The investigators attributed the poor performance of the oxygen-containing film to the possibly less corrosion resistant areas in the deep voids and microcracks between the columns.

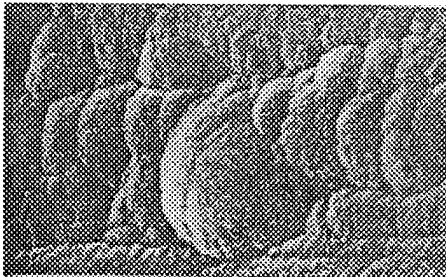
The N-containing alloy evaluated by Thakoor et al. [29] was fabricated with a 5:2 µm Ar- N_2 working gas ratio and exhibited a polycrystalline, nonporous, densely packed, columnar microstructure. The surface morphology of this material was also rough, similar to the zone 1 film deposited in pure Ar, described above. Thakoor et al. [29]



(a)



(b)



(c)



(d)

Figure 7. a Si:H film growth over a mechanically roughened KCl substrate with film thicknesses of (a) 1200Å, (b) 3000Å, (c) 1 μm , and (d) 10 μm , showing the morphological effects of a scratch on the substrate for various thicknesses of the overlaid deposit [22].

believed that as a result of the polycrystalline nature of the alloy, corrosion resulted from the numerous grain boundaries present in the void regions. These boundaries acted as less corrosion resistant areas and, thus, were the nucleation sites for breakdown.

As-Deposited Defects

A discussion of as-deposited surface defect morphology was presented earlier. These defects commonly take the form of scratches, holes, or protrusions which may act as nucleation sites provoking early breakdown of the passive film [8,27]. Furthermore, the irregularity of these defects has led to wide variations in breakdown potentials between 2 specimens removed from the same thin-film alloy [8,27]. For example, Schrecengost et al. [8] observed that the breakdown potential (E_b) of an Al-26%W alloy in a 0.1M Cl⁻ solution was considerably less than that of Al-10%W. According to the literature, the Al-26W should have the highest breakdown potential since E_b increases with increasing W concentration in the bulk alloy [6]. However in this case, the Al-10W alloy was fabricated in a class 100 clean room, whereas, the Al-26W alloy was fabricated in a lab environment. Thus, dust particles had a higher probability of collecting on the substrate of the Al-26W alloy prior to film deposition than on the alloy fabricated in the clean room. These particles on the surface were believed to affect film growth, with the overlaid deposit reflecting or magnifying the initial feature of the deposit, resulting in the presence of microscopic defects within the deposit which provoked early breakdown (pitting) of the alloys.

Breakdown may occur at the defect itself, possibly as a result of nonuniform growth of the alloy or the oxide barrier layer. However, another source [17] stated that film defects may cause a redistribution of stress in the alloy, which may possibly cause localized stress points or stress gradients across a film. These localized stress points may also act as nucleation sites for early breakdown.

EXPERIMENTAL PROCEDURES

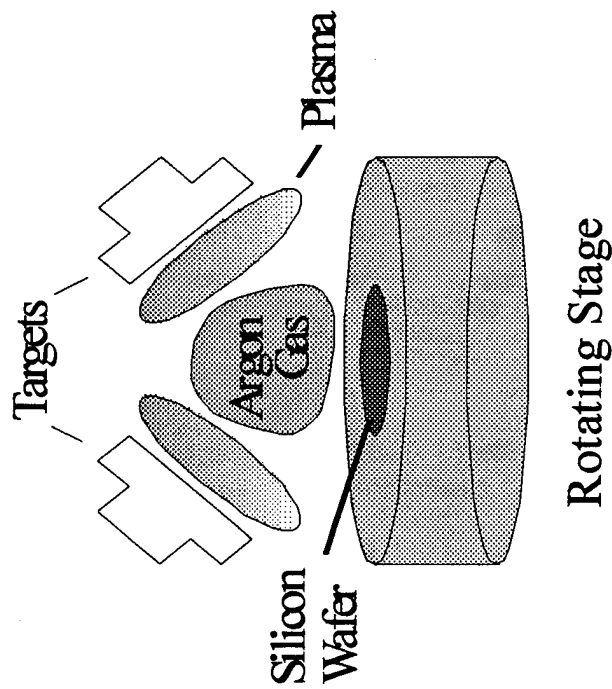
Pure Al, Al-Mo, and Al-W sputtered thin-film alloys with both constant and graded solute concentrations were prepared using a system built at Penn State. In this system, a 10-inch distance separates the substrate and the targets, and the substrate is mounted vertically. Base pressures were typically in the low 10^{-5} to 10^{-6} Torr range during deposition. The Al target power was maintained at either 240 W or 120 W, and the power of the solute target was changed to produce the desired atomic concentrations. Compositionally graded films were prepared by linearly increasing the solute power during deposition so that the highest solute concentration was on the outer layer of the deposit. The metal films were deposited onto either polished doped Si or oxidized doped Si wafers, and the substrates were rotated at a rate of approximately 4.5 revolutions/minute. In a limited number of experiments, SiO₂ substrates were used to eliminate galvanic coupling of the deposited film and substrate during anodic polarization tests. A previous study showed minimal changes in the thin-film microstructure with varying substrate types [30]. Thus, minimal microstructural variations were expected between films deposited onto Si with those deposited on SiO₂. The pressure of the Ar working gas was maintained at 6.0 mTorr during deposition. Deposition times varied from 30 to 120 minutes and substrate

temperatures during fabrication reached approx. 75°C. Measured film thicknesses were in the range of 0.3 μm to 0.8 μm . A schematic of the sputter deposition process is presented in Figure 8 a.

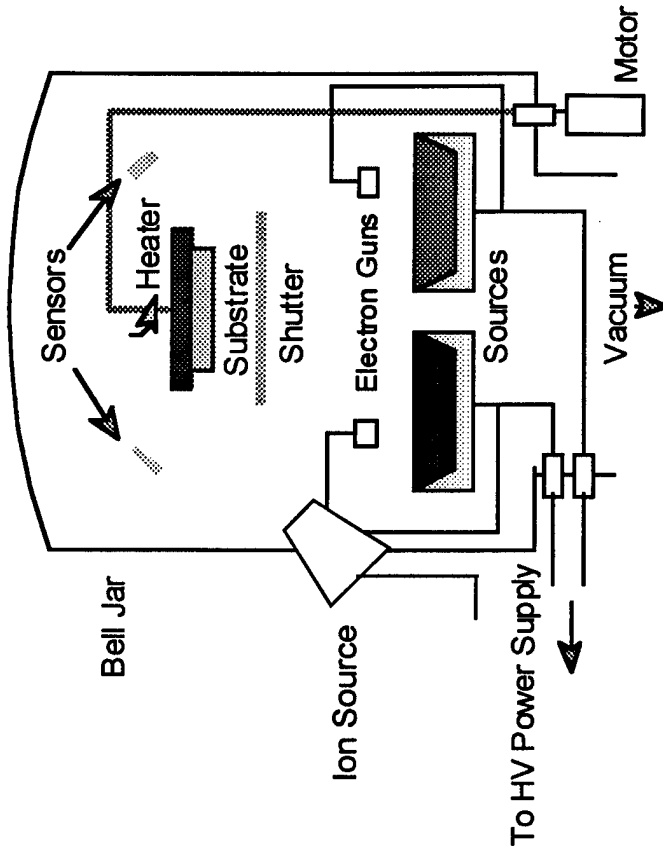
The high-rate physical vapor deposition facilities at INEL were used to fabricate e-beam evaporated Al-Mo alloys for evaluation. The deposition system consisted of two 15 kW Telemark electron beam guns mounted in a cryogenically pumped vacuum chamber. An Inficon Model 4 Plus deposition controller with dual crystal heads was used to monitor deposition rates in-situ. A 5-cm ion source was also mounted within the chamber for surface modification and substrate preparation. The system is schematically depicted in Figure 8 b. Molybdenum was chosen as the initial alloying element for the vapor deposited films since previous research revealed that it greatly enhanced the corrosion resistance of the sputter-deposited films and because its lower melting and vaporization temperatures allowed for more controlled e-beam evaporation. In addition, the density of Mo is lower than W which translates to lower density alloys.

The electron beam physical vapor deposited (EBPVD) Al-Mo alloys were evaporated onto glass and 1100 Al alloy substrates to thicknesses of 5 μm and 20 μm , respectively. The glass substrates were cleaned and degreased with ethanol prior to deposition. Aluminum substrates were prepared for deposition by sanding with 600 grit paper followed by chemically polishing with phosphoric acid solution at 80°C. Again, ethanol was used to degrease these substrates after polishing. Ion beam bombardment at an acceleration voltage of 300 V was used to remove the air formed oxide on the aluminum substrates for 15 minutes prior to deposition. Aluminum and Mo were co-evaporated in the dual gun e-beam system onto substrates rotating at 60 rpm. The Mo content of the alloys was controlled via a feedback system. Specimens with Mo contents of 2, 3.9, 5.7, 7.4, 9.1 and 10.7 volume percent ($\text{vol}\%$) (as determined by deposition rates) were produced for evaluation. Low energy ion beam bombardment with Ar and N was used on some specimens to modify the deposit during deposition. The ion beam current was set to 10 mA, with a beam voltage of 300 V, and RF power of 80 W for Ar ions. The RF power was set at 85 W for the N ions as it is more difficult to ionize than Ar. The temperature of the substrate was monitored throughout the deposition run. Table 1 summarizes the deposition parameters and estimated solute concentrations for the EBPVD specimens.

All of the constant solute sputter-deposited alloys were compositionally analyzed using direct current plasma spectroscopy (DCP). The composition of at least two samples of each alloy were measured and the average of the values is the composition reported. The initial and final compositions of the graded samples were estimated based on the concentration of the constant solute alloys fabricated at the same powers. In this study, total Mo concentrations ranged from 3 to 11 atomic percent, and total W concentrations ranged from 3 to 32 atomic %. Concentrations given in this report for the sputter-deposited alloys are in atomic percent, $\text{at}\%$, unless otherwise noted. DCP analysis has not yet been conducted on the e-beam evaporated alloys. (Note that the estimated solute concentrations for the EBPVD Al-Mo alloys are given in volume percent, rather than in atomic percent.)



(a)



(b)

Figure 8. Schematic representation of the systems used to fabricate nonequilibrium alloys: (a) magnetron co-sputter deposition system at Penn State Materials Research Laboratory, and (b) electron beam physical vapor deposition system (EBPVD) at Idaho National Lab.

Table 1 Summary of Deposition Data for EBPVD Al-Mo Alloys

Sample #	Substrate	Thickness μm	Max Temp $^{\circ}\text{C}$	Vol.%Mo	Precipitates	Ion Assist
ALM027	1100 Al	20.1	370	10.7	YES	N ₂
ALM026	1100 Al	20.2	361	10.7	YES	Ar
ALM025	1100 Al	20.1	350	10.7	YES	none
ALM024	Glass	2.8	143	10.7	ND*	none
ALM023	Glass	5.1	255	10.7	NO	none
ALM022	Glass	5.0	212	10.7	ND	none
ALM021	Glass	5.1	218	10.7	ND	none
ALM020	Glass	2.5	187	10.7	ND	none
ALM019	Glass	5.0	266	10.7	ND	none
ALM018	Glass	5.0	269	10.7	ND	none
ALM017	Glass	5.0	238	9.1	NO	none
ALM016	Glass	5.0	253	9.1	ND	none
ALM015	Glass	5.0	313	9.1	YES	none
ALM014	Glass	5.1	231	9.1	NO	none
ALM013	Glass	5.0	249	7.4	NO	none
ALM012	Glass	<1 μ	ND	7.4	ND	none
ALM011	Glass	<1 μ	ND	7.4	NO	none
ALM010	Glass	0.3	80	7.4	ND	none
ALM09	Glass	5.0	226	7.4	ND	none
ALM08	Glass	5.0	227	7.4	ND	none
ALM07	Glass	5.3		7.4	ND	none
ALM06	Glass	5.0	228	7.4	ND	none
ALM05	Glass	5.3	270	7.4	ND	none
ALM04	Glass	5.1	174	5.7	NO	none
ALM03	Glass	5.0	150	3.9	ND	none
ALM02	Glass	5.0	150	2.0	ND	none
ALM01	Glass	10.9	231	2.0	ND	none

*ND = Not Yet Determined

Polarization data were acquired on the sputter and vapor deposited alloys using either an EG&G Princeton Applied Research (PAR) Model 273 Potentiostat interfaced with a computer controlled by PAR Softcorr corrosion software (Model 352) or a Gamry PC3 interface board controlled by Gamry CMS100 system software. Tests were conducted at room temperature in a quiescent 0.1M NaCl solution that was initially adjusted to a pH of 8 with NaOH. Most experiments were conducted at a scan rate of 0.2 mV/sec; however, a few experiments were conducted at a slower rate to determine if scan rate influenced breakdown potential. Electrochemical specimens were prepared by attaching a lead wire and painting the backs and edges of cleaved segments of the wafer with a marine epoxy paint (Interlux 404/414) so that only the alloy surface was tested. EBPVD specimens were tested in a flat cell type corrosion flask with electrical contact made on the front face of the specimens deposited on glass.

As-deposited and polarized films were characterized using one or more of the following: optical microscopy, high resolution scanning electron microscopy (HSEM), or scanning laser microscopy (SLM). Each as-deposited film was carefully examined for any possible surface defects that could alter the polarization behavior, and polarized samples were examined to characterize breakdown sites. Optical microscopy was performed before and after each anodic polarization using a Cambridge Instruments Stereo Zoom 7 microscope with variable magnifications from 10X to 70X. A Lasertec SLM model 1LM11 was used for characterization of as-deposited films at magnifications of 245X to 4635X. Additional capabilities of this instrument include measurements of widths and depths of surface features. A high resolution scanning electron microscope, an ISI dual stage Model 130, was used for topographic and cross-sectional analyses of the thin-film alloys at high magnifications of 20,000 to 50,000 times.

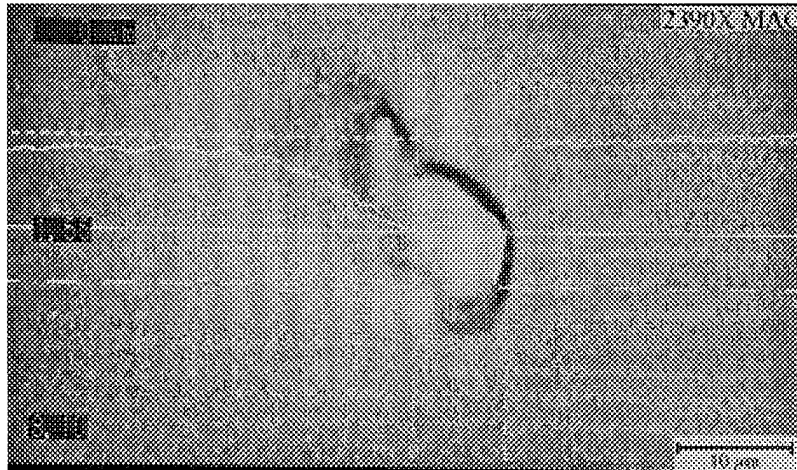
X-ray diffraction was used to determine if the deposits were crystalline or amorphous and to identify crystalline phases. Both Phillips and Scintag diffractometers were used in these studies and both systems utilized a copper K_{α} radiation source.

RESULTS AND DISCUSSION

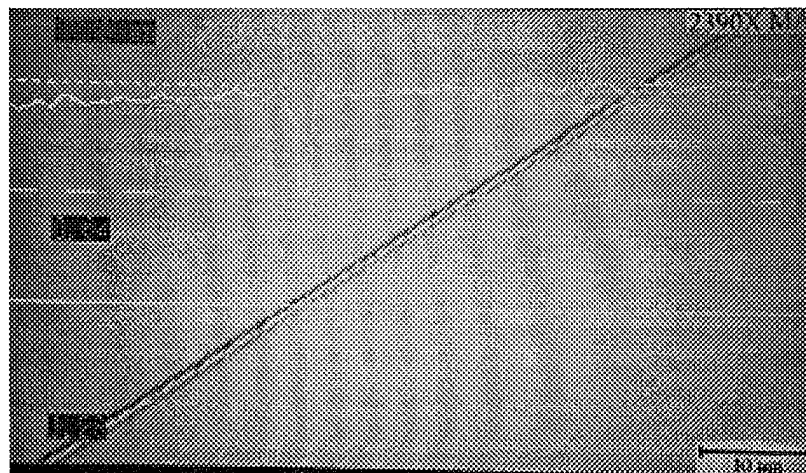
Alloy Characterization

Sputter-Deposited Thin-Film Alloys

Characterization of as-deposited sputtered alloy surfaces, using the SLM, indicated that almost all of the thin-film alloys contained surface defects, such as the ones shown in Figure 9. These defects included: scratches, holes, interconnected voids, and surface protrusions. Micrographs presented in last year's report summarized the range of defects observed to date in the sputter deposited thin-film alloys. [28] The presence of these anomalies is important because they have been found to act as pit initiation sites. [8,27,31-33] An in-situ SLM micrograph showing pitting on scratches in an Al-14%Mo sputter deposited alloy during anodic polarization in 0.1M NaCl is shown in Figure 10. Similarly, Figure 11 shows an SLM micrograph revealing pitting which occurred on a scratch in a pure Al film. Whether or not an anomaly acts as an initiation site is dependent on the severity of the anomaly. The insert in Figure 10



(a)



(b)

Figure 9. (a) scanning laser microscope(SLM) image showing a surface protrusion on a sputter-deposited alloy. (b). SLM image showing a scratch on the surface of a sputter-deposited alloy.

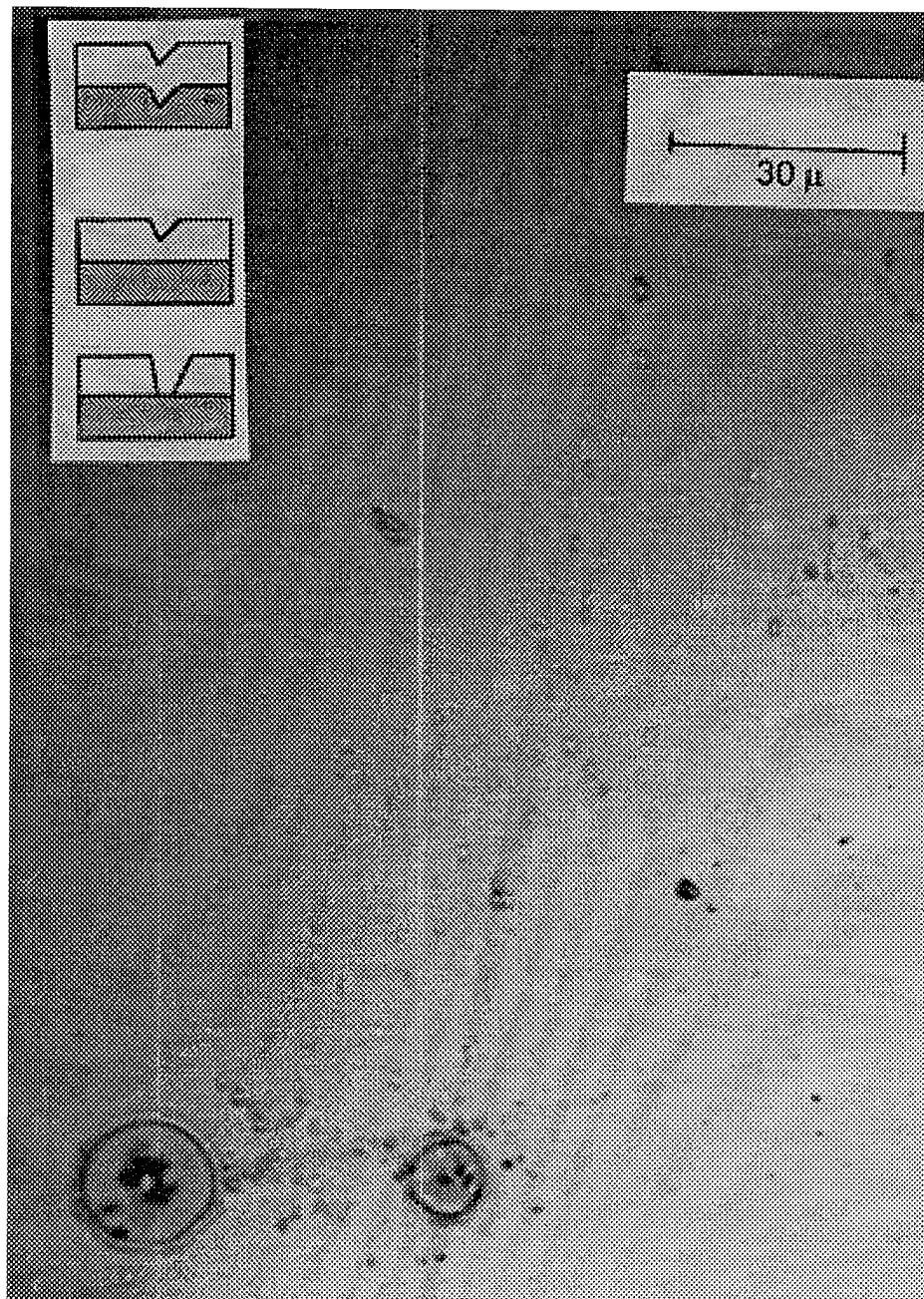


Figure 10. In-situ observation of pit initiation on scratches in a sputter-deposited Al-14Mo alloy anodically polarized in 0.1 M NaCl solution .

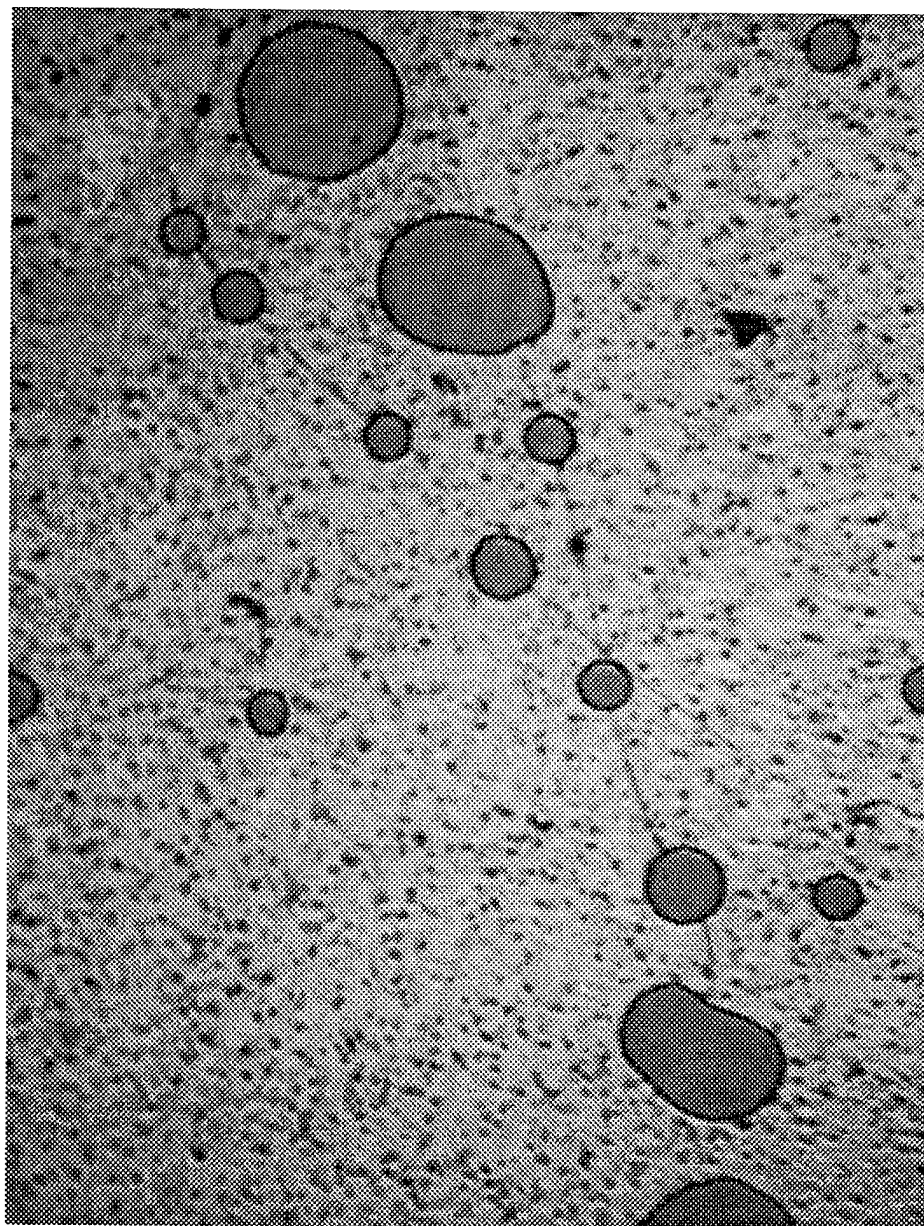


Figure 11. SLM micrograph of a sputter deposited pure Al film after anodic polarization in 0.1 M NaCl solution at pH 8 showing pitting on scratches.

schematically illustrates some possible cross-sectional views through a scratch. The bottom illustration in the insert shows a scratch which penetrates through the entire thickness of the film and exposes the substrate. This type of defect is considered to be detrimental to corrosion performance since some galvanic interaction may occur when the doped (semiconducting) Si substrate is exposed. In the middle illustration in the insert, the scratch only penetrates part way through the deposit. Scratches such as these are likely the result of damage incurred during the cleaving process or during handling of the cleaved specimens. During cleaving small fragments of Si are produced which are capable of cutting through the Al alloy thin-films. In addition, after cleaving small Si fragments are present at the edges of the cleaved wafer sections and these fragments can break loose during handling and further damage the alloy films. Defects such as the ones illustrated in the center insert may or may not affect corrosion performance, depending on the geometry of the scratch. The top illustration in the insert illustrates how a scratch in the underlying substrate influences film growth. The translation of these defects through the deposit can affect corrosion performance; again, the affect will depend on the geometry of the defect. Figures 12 and 13 show localized breakdown (pitting) on scratches which initiated on the substrate and translated through the deposit. Based on the pattern of these scratches, they appear to have resulted from polishing of the substrate. Substrate defects can also lead to shadowing effects which result in thin areas in the deposits. Defects such as the ones illustrated in Figures 9-13 are believed to be responsible for the wide variations in breakdown potential that are sometimes noted for replicate specimens taken from the same thin-film alloy. In support of this assertion, significantly higher breakdown potentials (several hundred millivolts) have been noted for alloys produced in a class 100 clean-room versus those produced in an ordinary lab environment.

Cross-sectional micrographs for Al240-Mo alloys (Al-Mo alloys deposited with a 240 W power setting on the Al target) at various Mo concentrations illustrating morphological changes with increasing solute concentration are presented in Figure 14. The pure Al, film shown in Figure 14 a, exhibited a compressed, relatively dense cross-sectional microstructure. Some columnar growth was detected, but it appeared that the columns had slightly coalesced. Furthermore, the surface of the pure Al was nonuniformly rough. Note that the smooth surface on the left side of the photo is the underside of the film; thus, indicating an extreme microstructural difference between the initial film growth and the final film layer. Figure 14 b shows a cross-sectional micrograph of an Al-3.4%Mo alloy. Columnar growth was more apparent in this alloy than in the pure Al and this columnar growth can be observed in the upper half of the film. In the next micrograph, Figure 14 c, the Al-5.5%Mo film exhibited distinct wide columnar growths throughout the entire film thickness. Figure 14 d shows the microstructure of an Al-9%Mo alloy revealing a dense, compact profile with columnar growth noticeable on the surface of the alloy. However, gaps or distinct boundaries between the columns in the cross-sectional view were nonexistent, giving the impression that the columns in this deposit had coalesced. The cross-sectional microstructure and topography of an Al-10.5%Mo alloy were found to be similar to those of the Al-9%Mo alloy. Comparison of the surface morphologies for the Al-Mo alloys revealed that the Al-9%Mo film was much smoother than the others. Deep, wide grooves were observed between the columns in the pure Al, Al-3.4%Mo, and Al-5.5%Mo films; whereas, only small, shallow grooves were present on the surface of the Al-9%Mo alloy.

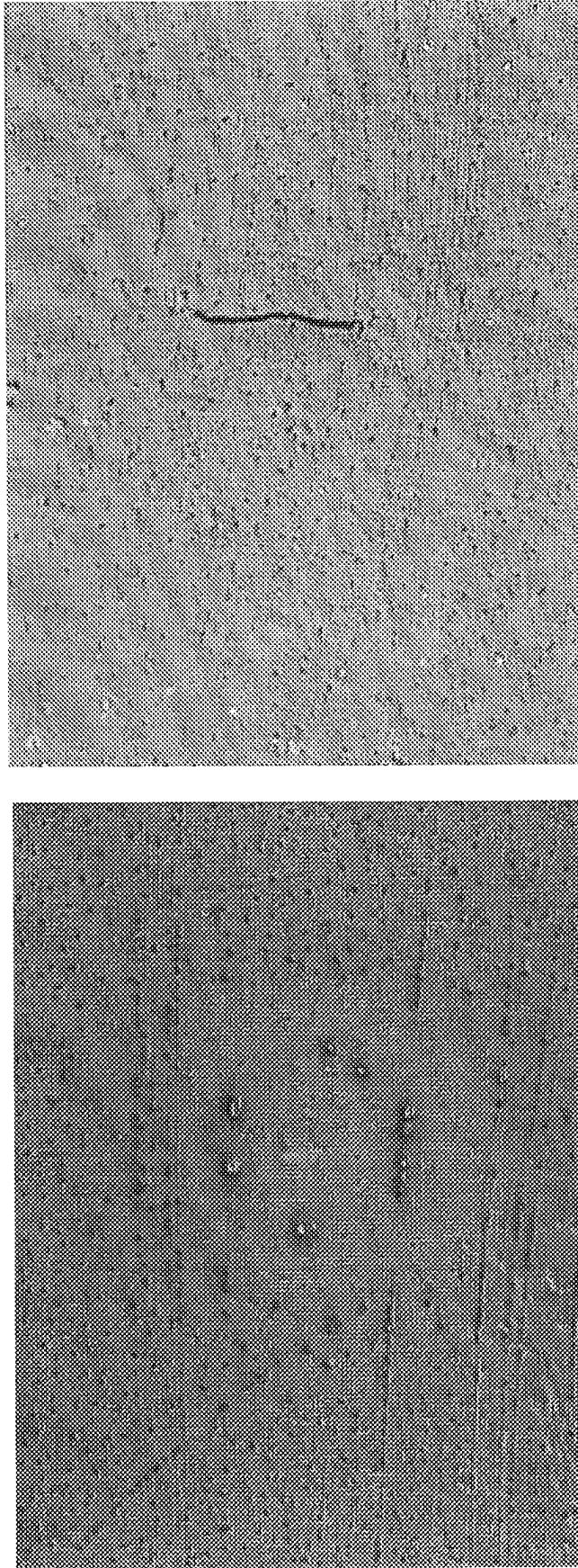


Figure 12. Two optical images showing pitting on polishing scratches evident on Al-Mo specimens after polarization.

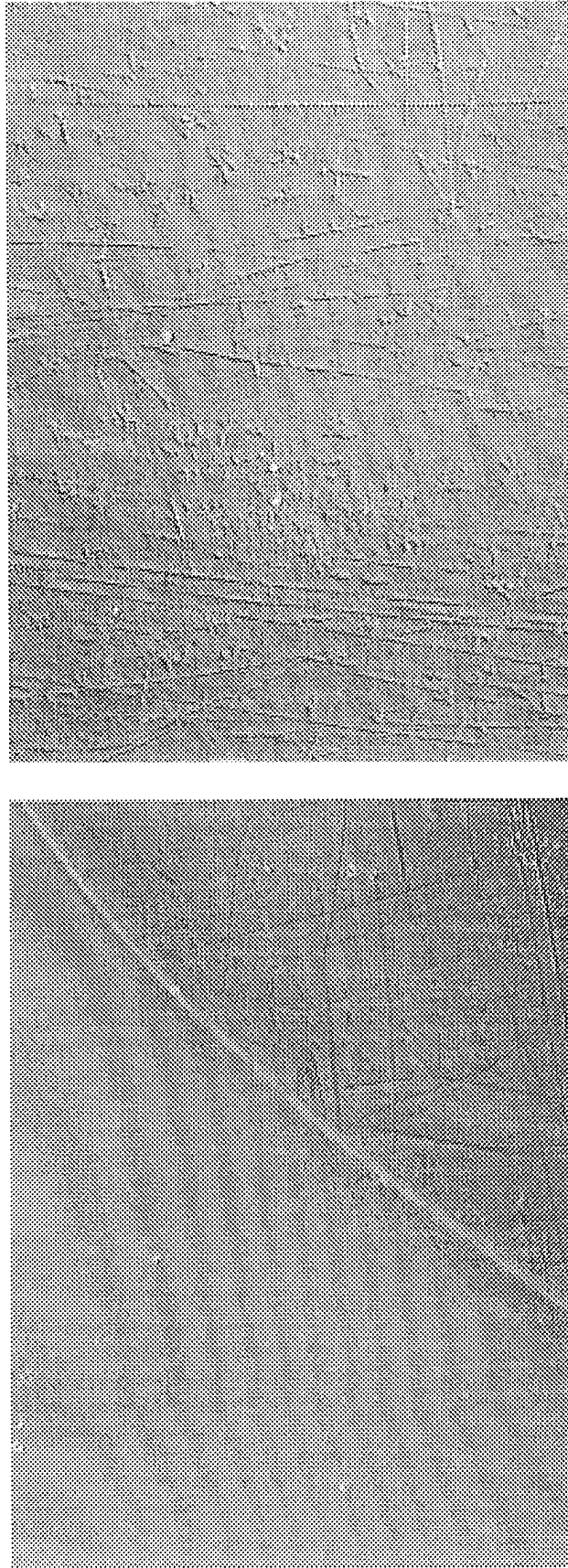


Figure 13. Two optical images showing pitting on polishing scratches evident on Al-Mo specimens after polarization.

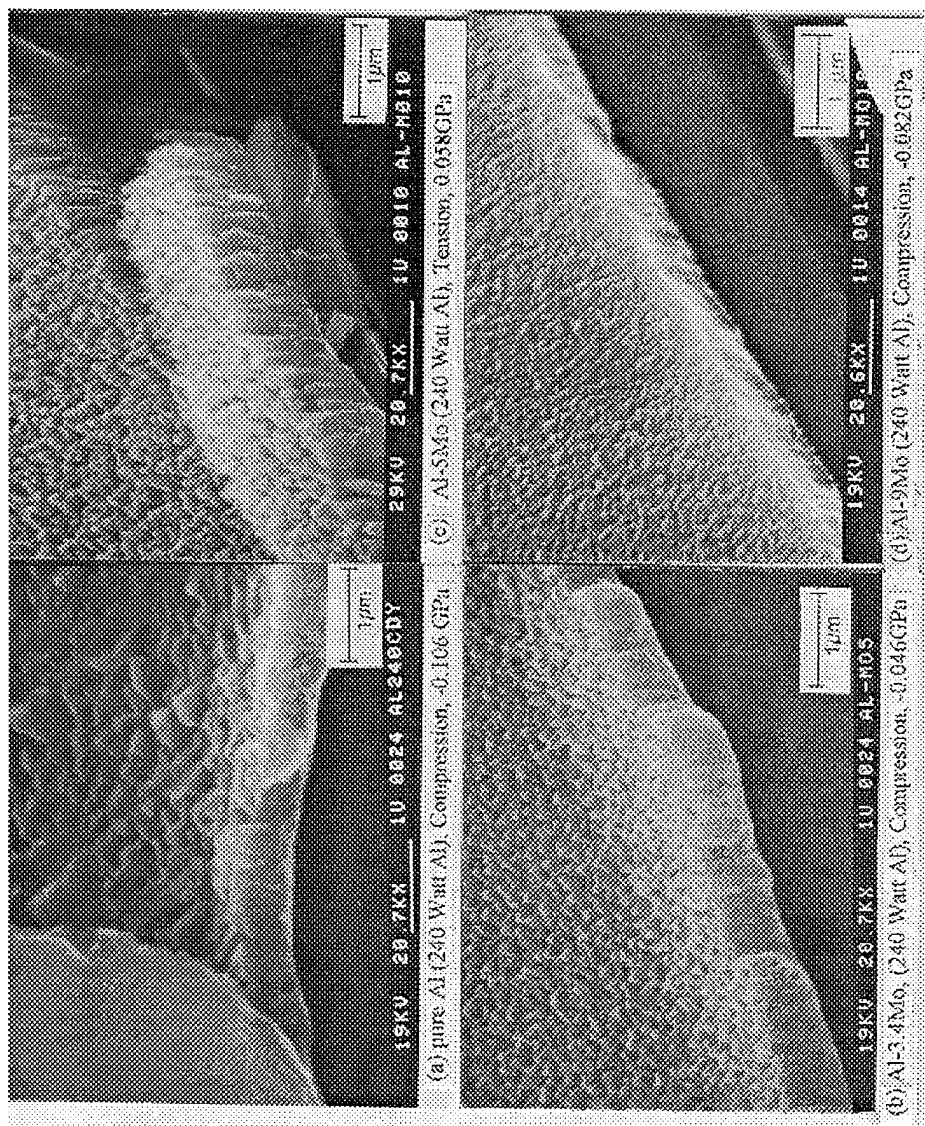


Figure 14. Cross-sectional SEM images depicting various morphologies of Al-Mo thin film alloys produced with 240 W of power applied to the Al target and a varying wattage on the Mo target:
a) pure Al, b) Al-3.4at/o Mo, c) Al-5at/o Mo, and d) Al-9at/o Mo.

Cross-sectional and surface micrographs for the Al-W alloys, at several different W concentrations deposited at a power setting of 240 W on the Al target, are presented in Figure 15. The microstructure of the pure Al sputtered film was discussed earlier and is shown, again, in part a of Figure 15 for comparison purposes. Alloys with 6.6 and 7 %W are displayed in Figures 15 b and 15 c, respectively, and reveal very similar microstructures. Both alloy films had stresses close to zero, but the Al-6.6%W alloy was in tension; whereas, the Al-7%W alloy was in compression. Both cross-sections showed distinct columnar growths separated by boundaries which were characteristic of zone 2 films in Thornton's SZM. Additionally, both alloys exhibited uniformly rough surface morphologies displaying deep grooves between the columns. When compared to the lower W concentration alloys, the Al-22%W alloy, which had a high tensile stress, revealed a significantly different morphology. The Al-22%W alloy exhibited columnar grain growth, but for this alloy the grains were much thinner and more compact, and the surface roughness was smoother than that of the other Al-W alloys. The Al-22%W alloy appeared to have a zone T microstructure possibly located near the zone T/zone 1 boundary.

Cross-sectional and surface micrographs for the Al-W alloys deposited at a power setting of 120 W on the Al target are presented in Figure 16. Figure 16 a, shows an Al-6%W alloy, revealing a very dense, compact microstructure. This alloy appeared to have a zone 1 microstructure possibly located near the zone 1/zone T boundary. The large mound located on this specimen's surface may be either the beginning of a hillock or preferential growth possibly caused by a contaminate on the surface prior to sputtering. The cross-sectional microstructures of the Al-10.8%W alloy, the Al-18.5%W alloy, and the Al-37.4%W alloy were clearly different than that of the compressed Al-6%W alloy. The three higher solute concentration alloys exhibited high tensile stresses. Small diameter columnar growth was apparent in these microstructures, and the topography of the alloys was smooth, signaling a zone T microstructure. However, a hint of surface structure was noted on the Al-10.8%W alloy; therefore, this alloy may actually lie near the zone 1/zone T boundary. Topographies for the Al-6%W and the Al-10.8%W films revealed that these alloys had a slightly more defined surface structure than the Al-18.5%W and Al-37.4%W alloys, consisting of small hills and small shallow grooves. The dark areas found on the surface of the Al-18.5%W alloy were attributed to a nonconductive deposit, such as grease, on the alloy surface.

The results presented above clearly indicate morphological changes in the alloys with increasing solute concentration. Thus, some changes in the morphology of a deposit should be expected for compositionally graded alloys. Figure 14 (a through d) revealed the morphological changes that could be expected with increasing solute concentration in an Al-Mo alloy. An example of the morphology of a graded Al-(3.4 to 9)%Mo alloy is presented in Figure 17 a. As expected, the initial morphology of this deposit was similar to that noted for the Al-3.4%Mo alloy (Figure 14 b). As the alloy grows and the solute concentration increases, the microstructure of the graded deposit is expected to change in a manner similar to that presented in Figure 14. Thus, the distinct columns seen in the microstructure in the mid-region of Al-(3.4 to 9)%Mo should reflect the morphology of Al-5%Mo (Figure 14 c). Finally as the film grows thicker, the microstructure of the graded Al-(3.4 to 9)%Mo deposit is expected to be somewhat similar to that of the Al-9%Mo deposit. This appears to be the case since the diameters of the columns increased, and the gaps separating these columns

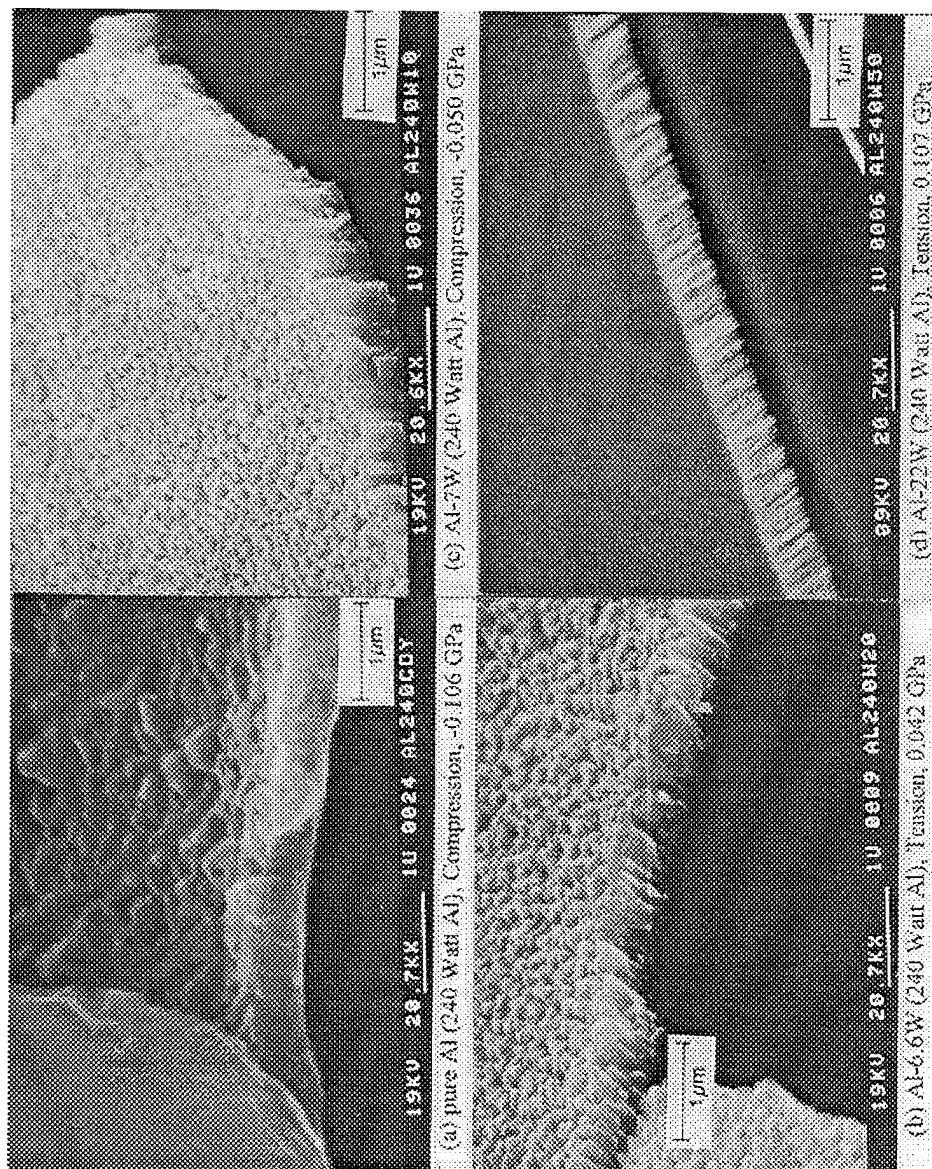


Figure 15. Cross-sectional SEM images depicting various morphologies of Al-W thin film alloys produced with 240 W of power applied to the Al target and a varying wattage on the W target:
a) pure Al, b) Al-6.6at/o W, c) Al-7at/o W, and d) Al-22at/o W.

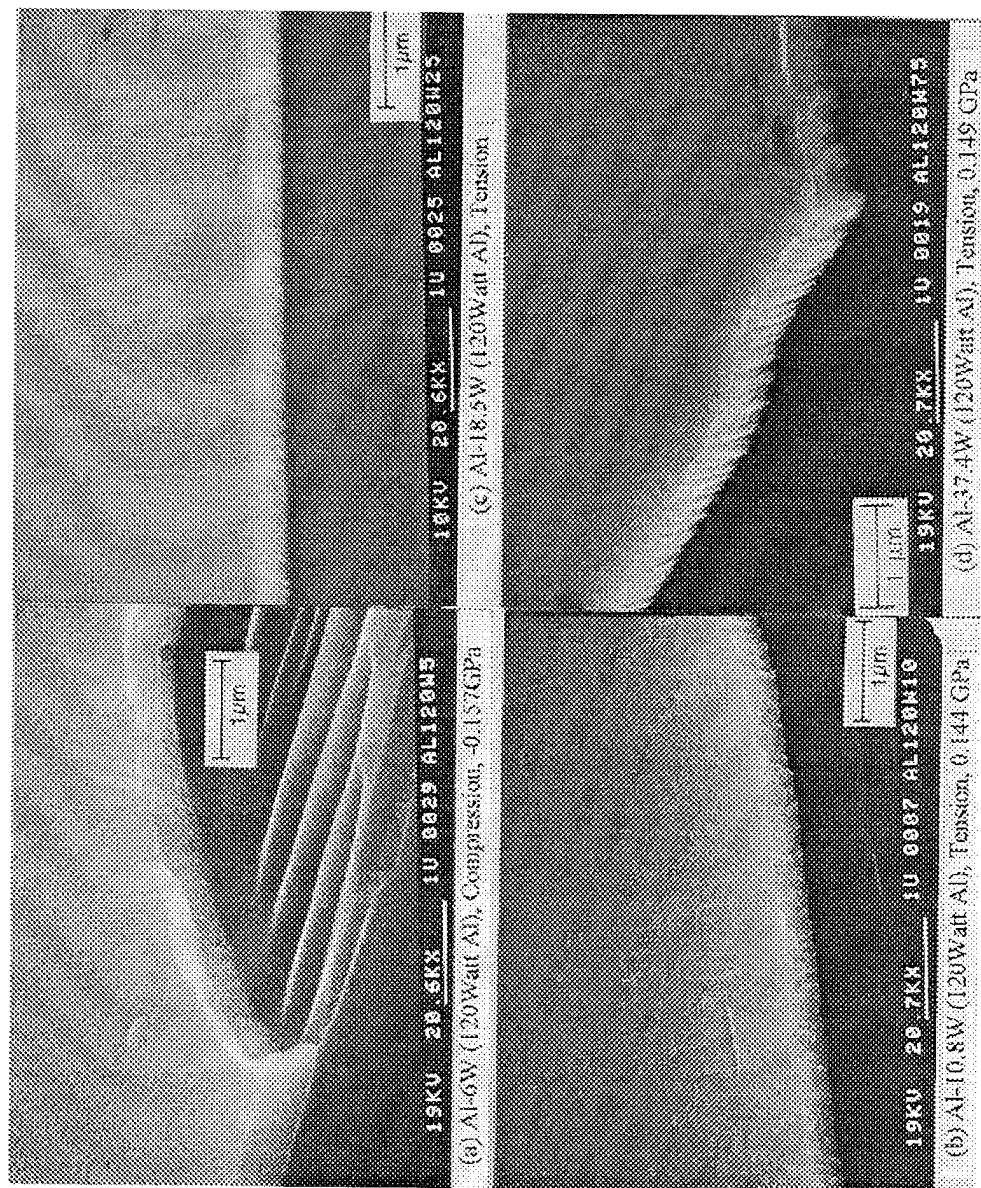
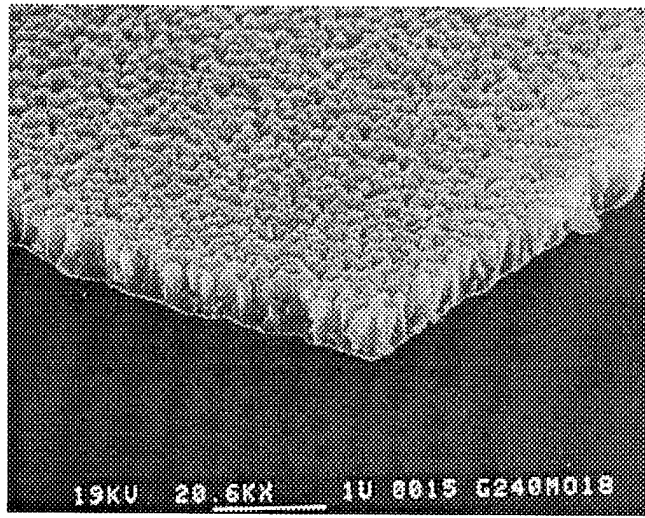


Figure 16. Cross-sectional SEM images depicting various morphologies of Al-W thin film alloys produced with 120 W of power applied to the Al target and a varying wattage on the W target:
a) Al-6at/o W, b) Al-10.8at/o W, c) Al-18.5at/o W, and d) Al-37.4at/o W.



(a)



(b)

Figure 17. Cross-sectional microstructures of compositionally graded, as-deposited Al-Mo alloys with Mo concentrations of:
(a) Al-(3.4-9)%Mo, (b) Al-(<0.5 to 5)%Mo

decreased. Figure 17 b shows the cross-section of an Al-(<0.5 to 5)%Mo alloy and reveals a microstructural gradient similar to that observed in part a of this figure. However in this case, only the microstructures in Figures 14 a, b, and c are consecutively apparent as seen by the graded film's undefined columnar base and its distinct columnar structure in the bulk and on the surface of the film.

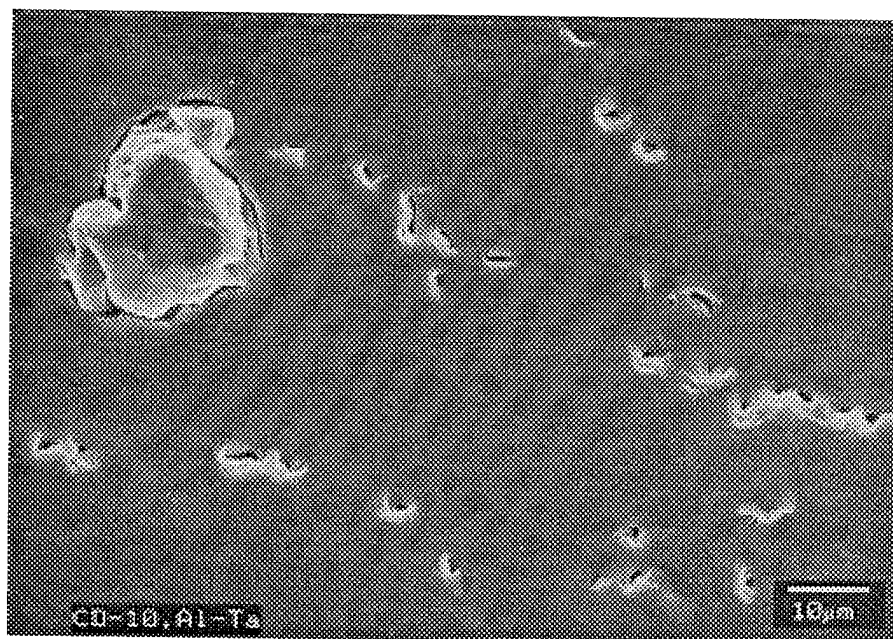
X-ray diffraction of the sputtered thin-film alloys revealed that all of the Al and Al-Mo films, both graded and constant compositions, were crystalline. In contrast, all of the sputtered Al-W alloys, with the exception of the lowest solute concentration alloy, were amorphous. No evidence of Mo or W precipitates was found.

Electron Beam Physical Vapor Deposited (EBPVD) Thin-Film Alloys

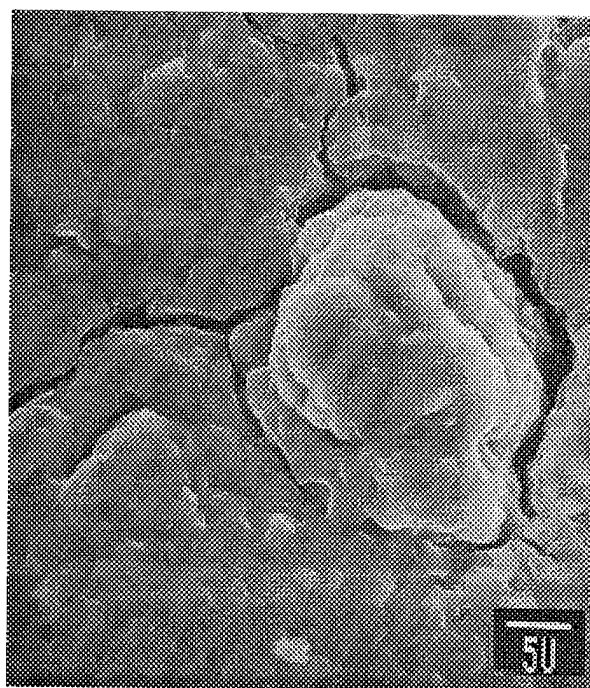
Previous research on Al-W and Al-Ta EBPVD alloys revealed the presence of nodules and large crevices within the deposits as illustrated in Figure 18. The nodules were determined to be the result of the incorporation of fragments of solute target within the deposit. It was believed that defects in the solute rod stock target led to the ejection of fragments of the solute metal during initial e-beam melting. These nodules are concern for two reasons. First, depending on when the particles were ejected and whether they were subsequently coated with the alloy, their presence could establish localized galvanic couples on the surface of the deposit -- leading to preferential dissolution of the alloy adjacent to these nodules. Second, the nodules disturb subsequent film growth; leading to the possible establishment of large, surface connected crevices in the deposit, such as the one visible in Figure 18 b. Other crevices or grooves were noted in some of the earlier deposits and were linked to the presence of small particles on the substrate or roughness of the substrate. Both of these types of defects are illustrated in the micrographs presented in Figure 19.

Initial studies revealed that nodules in the deposit could be avoided if the target stock was completely melted and resolidified prior to deposition. In addition, these initial studies showed that a smoother surface finish for the substrate alleviated the crevice problem. Optical cross-sections through the 20 μ m thick vapor deposited Al-11v/o Mo alloy revealed a uniformly dense region adjacent to the substrate and a columnar structure toward the surface of the deposit. Some second phase precipitates could also be observed in some of the optical micrographs. Figure 20 shows a typical cross-section of a vapor deposited Al-11v/o Mo alloy on an 1100 series Al substrate. This micrograph revealed that the initial growth of the film was dense with no apparent columnar structure, but later growth resulted in a well defined columnar structure. This type of growth pattern is not uncommon in relatively thick sputter and vapor deposits and the rationale for this type of growth was discussed earlier in the background section of this report. Optical and SEM inspection of the EBPVD alloys revealed the presence of small pin holes in many of the deposits. For two of the EBPVD alloys, ion bombardment was used during deposition in an attempt to further densify the deposit. An optical cross-section through one of these ion beam assisted deposits is presented in Figure 21. Unfortunately, some technical problems with the ion gun resulted in deposits which did not exhibit increased density.

X-ray diffraction of the vapor deposited films showed sharp peaks corresponding to Al in all of the alloys, indicating that the deposits were crystalline. The location of the Al

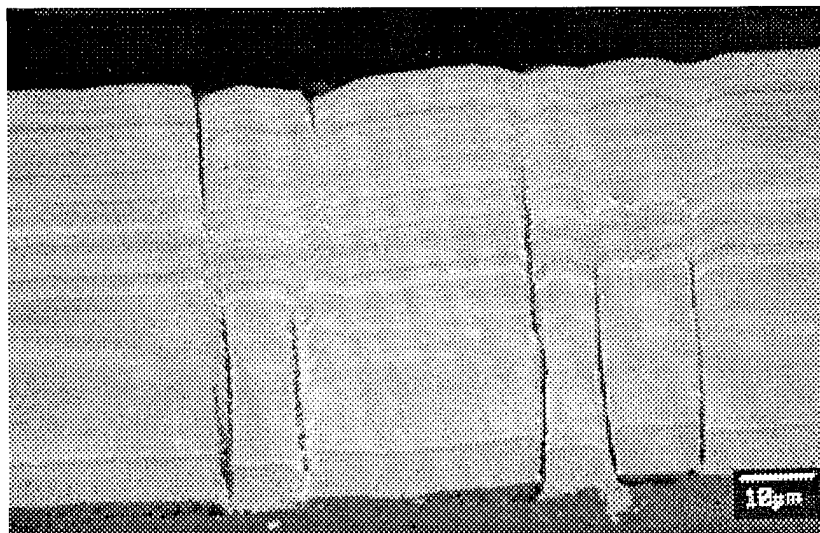


(a)

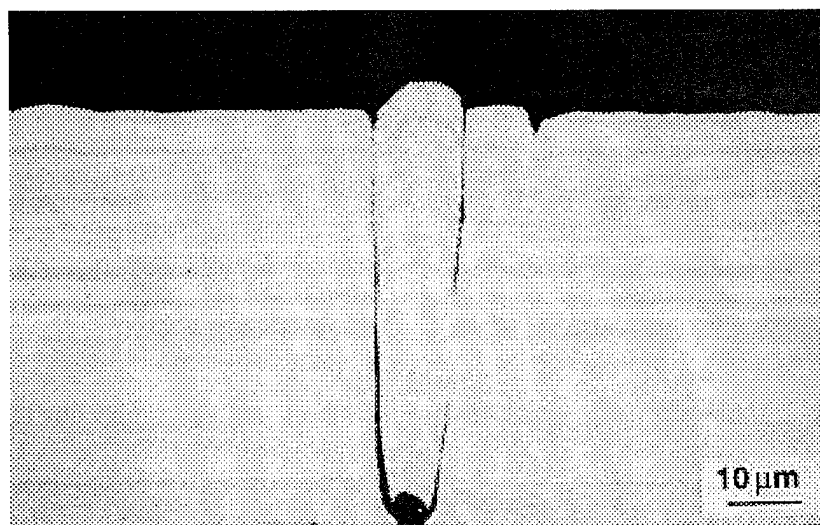


(b)

Figure 18. SEM micrographs of early EB-PVD alloys:
a) surface of Al-Ta alloy showing nodule and crevices on the deposit surface and b) a higher magnification image of the Al-Ta surface showing crevice surrounding the nodule.



(a)



(b)

Figure 19. Cross-sectional SEM micrographs of an EB-PVD Al-Ta film showing: a) grooves/crevices in the deposit resulting from roughness of the substrate surface, and b) a groove/crevice in the deposit resulting from a particle on the substrate surface.

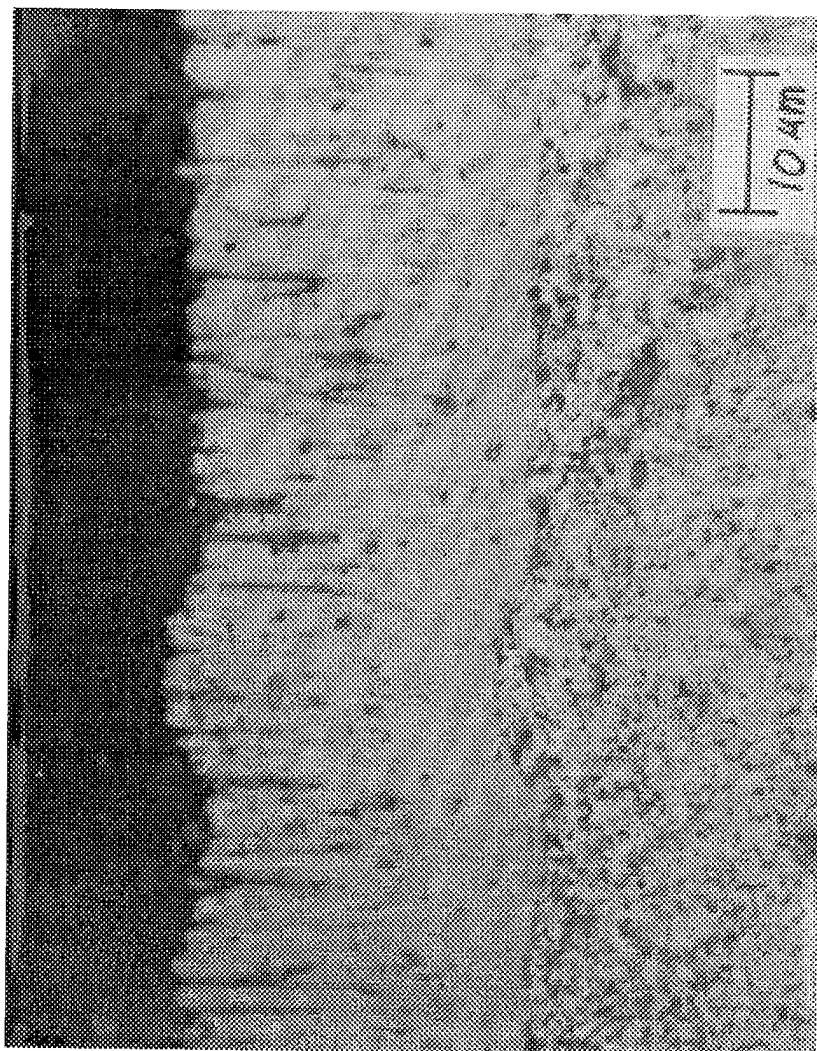


Figure 20. Cross-sectional SEM micrograph of an EB-PVD film showing initial dense growth of the deposit followed by columnar growth.

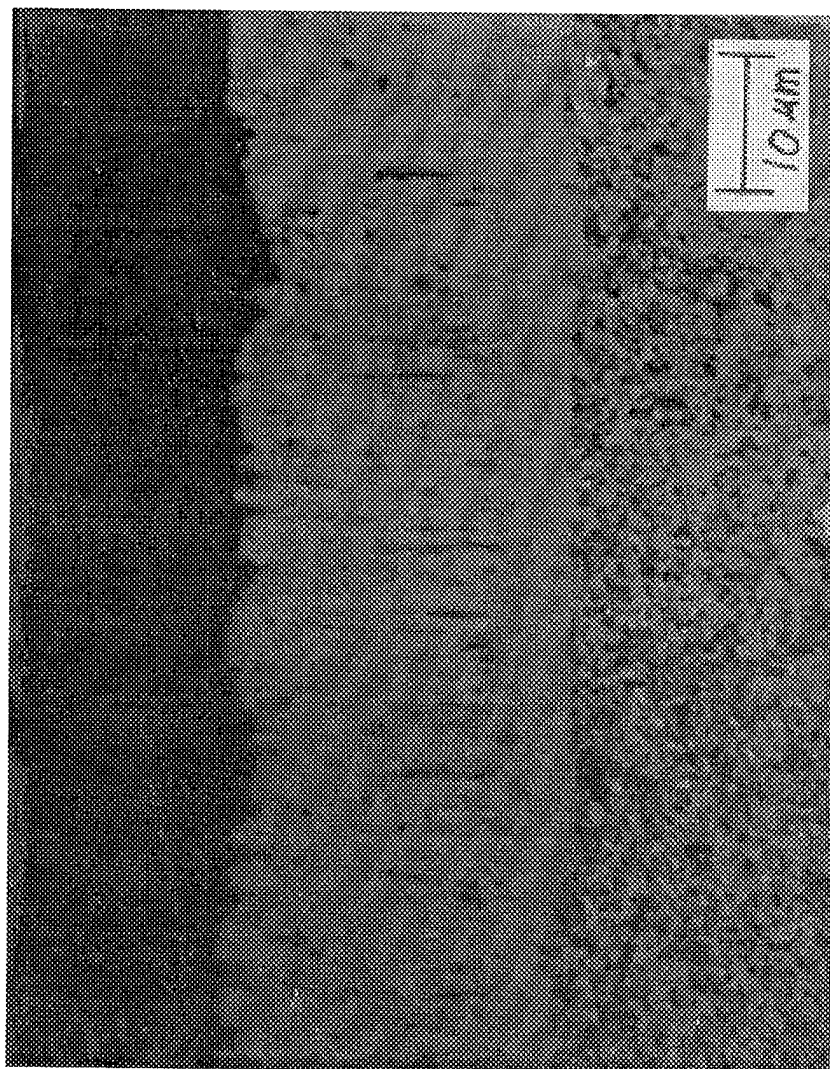


Figure 21. Cross-section SEM micrograph of an ion beam assisted EB-PVD film showing cross-sectional morphology of the deposit.

diffraction maxima were shifted to the right of the peak locations for pure Al, indicating that the Mo had formed a solid solution with the Al. A typical diffraction pattern for one of the Al-11v/o Mo vapor deposited alloys is shown in Figure 22. In some alloys, additional diffraction maxima were observed. These additional diffraction peaks were corresponded to those of Al_{12}Mo . A typical diffraction spectra for one of these precipitate containing alloys is presented in Figure 23. Alloys which reached temperatures in excess of 300°C during deposition were found to contain the Al_{12}Mo precipitates. This observation of precipitation at temperatures in excess of 300°C was consistent with work conducted by the Royal Aerospace Establishment on vapor deposited Al-Cr-Fe alloys where precipitation was observed at temperatures in excess of 250°C . A summary of the x-ray diffraction results for the EBPVD alloys was included in Table 1 which was presented earlier in the experimental procedures section of this report.

Zone Changes with Increasing Solute Concentration for Sputtered Alloys

The results of this research revealed that the sputtered Al alloys exhibited a semi-unique zone change with increasing solute concentration. For example in the Al-W alloys deposited with a power setting of 240 W on the Al target, the microstructure changed from the zone 2/zone 3 boundary to a zone 2 microstructure and then to a zone 1 smooth surface microstructure with increasing solute concentration. Similarly, the Al-Mo alloys switched from a zone 2/zone 3 boundary to a zone 2 microstructure and then to a zone 1 rough surface microstructure. On the other hand, growth of the Al-W alloys deposited with a power setting of 120 W on the Al target initiated with a zone 1 rough surface microstructure and changed to a zone 1 smooth surface microstructure as W concentration increased.

Solute concentration was found to be a parameter that had a significant impact on the microstructure of the thin-film alloys. Changes in film microstructure with increasing solute concentration can be attributed to the following four concurrent phenomena: (1) an increase in sputtered species bombardment, (2) an increase in Ar reflected neutrals bombardment, (3) a rise in the melting temperature (T_m) of the deposited film, and (4) an increase in the number of nucleation growth sites. Figure 24 presents a schematic illustration of a modified structure zone model based on an article by Messier et al. [19] which indicates that the boundary between zone 2 and zone T increases in the reduced temperature direction as bombardment increases. This figure shows the different zones as a function of the homologous temperature, T/T_m , and bombardment, V_s ; where V_s (the substrate floating potential) is dependent on the sputtering gas pressure and the average energy of the deposited sputtered species. Note that the boundaries separating the zones are not discrete, instead they represent a continuous change from one zone to the next.

Mechanisms 1 and 2, listed above, could induce a microstructural zone change by increasing the adatom energy change resulting from atomic bombardment at the growing film surface. Since W is almost 7 times heavier than Al, and Mo is approximately 3.5 times heavier than Al, an increase in the solute concentration should cause an increase in the rate and impact energy of particles bombarding the growing film surface. These increases would result in the formation of a more uniformly

FN: ALMO23.NI	ID: ALUMINUM MOLY ON GLASS	SCINTAG/USA
DATE: 6/ 7/95	TIME: 8: 25	PT: 0.600
	STEP: 0.020	WL: 1.54059

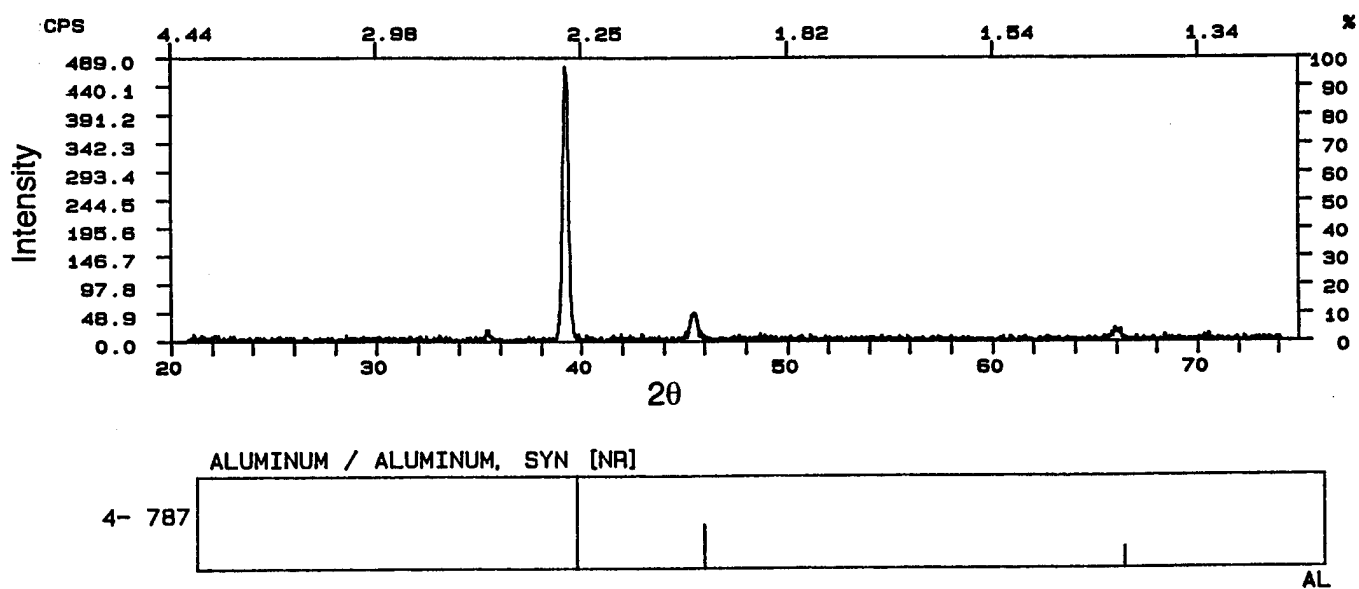
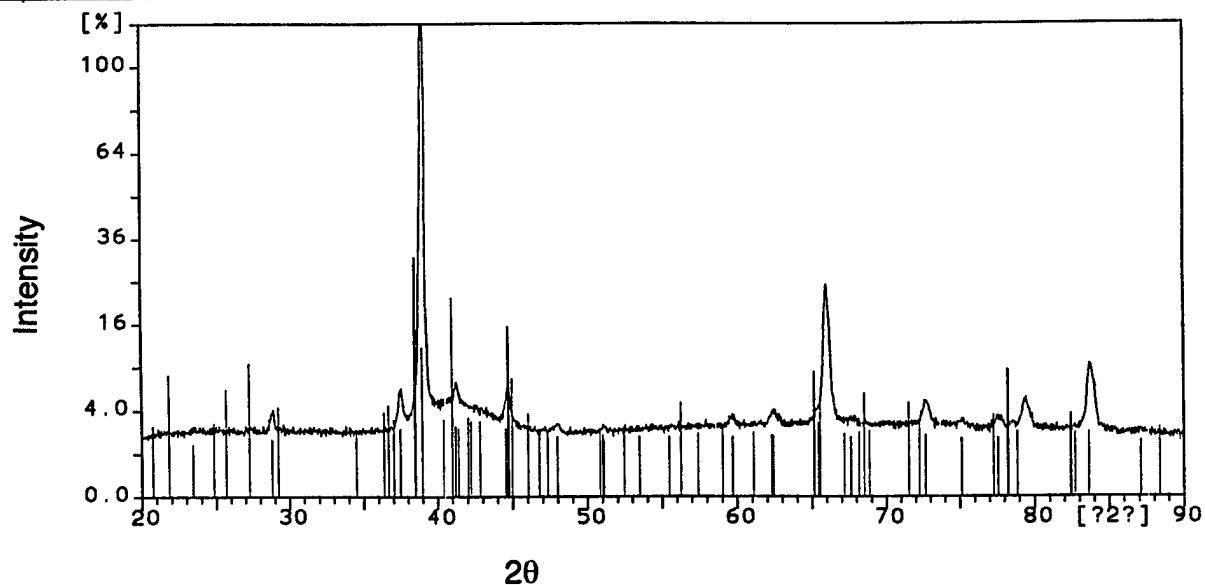


Figure 22. X-Ray diffraction (XRD) pattern for an Al 11 v/o EBPVD alloy.

Sample ident.: ALMo15

9-Nov-1994 9:45



Al12Mo
Al
Al5Mo
AlMo3

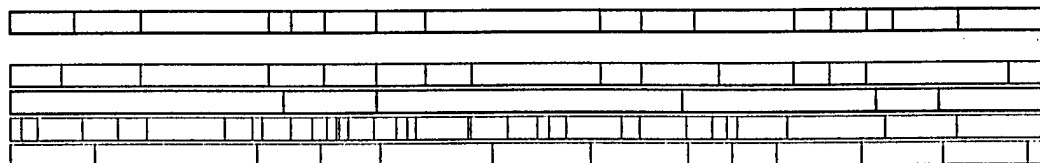
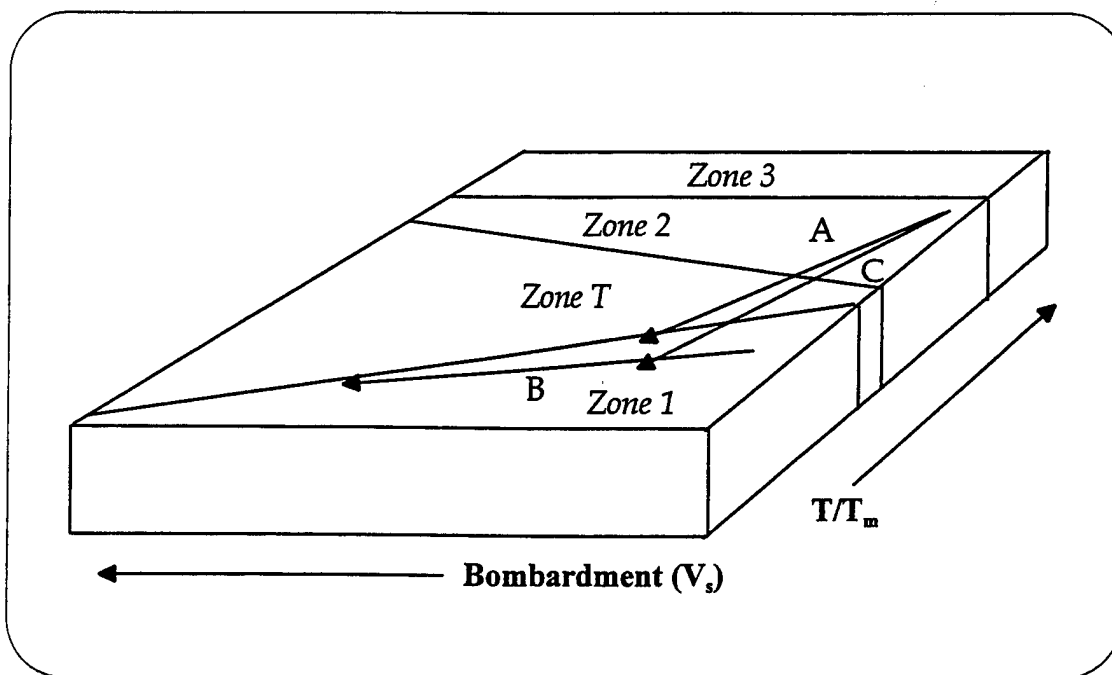


Figure 23. X-ray diffraction (XRD) pattern for an Al-9 v/o Mo EBPVD alloy.



**Figure 24. Modified structure zone model showing zone transition as solute concentration increases:
 line A for Al240-W alloys,
 line B for Al120-W alloys,
 line C for Al-Mo alloys.**

dense film. Additionally, since the atomic mass of Ar is much less than that of W, or Mo, elastic collisions at the solute target may occur, possibly causing reflected Ar neutrals to bombard the growing film. As the power on the solute target was increased, the rate and velocity of the Ar reflected neutrals also increased -- further densifying the coating. Theoretically, the reflected Ar neutrals should mostly result from the W or Mo target since Al has a molecular mass less than Ar. Therefore, varying the power on the Al target from 120 W to 240 W will have little influence on the bombardment energy or rate of the reflected Ar neutrals. In combining mechanisms 1 and 2, a lateral zone transition is expected to occur along the bombardment axis, V_s , in the structure zone model, as shown in Figure 24.

Mechanisms 3 and 4, listed above, may also influence film microstructure. As the solute content in the alloy is increased, the film growth nucleation sites could possibly become smaller and more abundant. Therefore, the film would be expected to become denser and yield a zone T microstructure. An increase in solute concentration also increases the melting point of the alloy, thus lowering the homologous temperature. As a result, the fourth proposed mechanism would cause a longitudinal zone transition along the homologous temperature axis. The consolidation of the four mechanisms discussed above would result in a zone transition somewhat similar to paths of line A for Al240-W alloys, line B for Al120-W alloys, and the line C for Al-Mo alloys in Figure 24.

The compressed zone 1 microstructures of the Al-9%Mo and Al-10.5%Mo alloys showed no columnar growth in their cross-sections; whereas, the tensile zone 2 microstructure of the Al-5%Mo alloy exhibited distinct columnar growth. The change in stress state from tension for the Al-5%Mo alloy to compression for the Al-9.5%Mo alloy may have been caused by an increase in surface mobility resulting from an increase in the average energy of the bombarding sputtered species. This increase in energy of the bombarding species would promote a complete coalescence of the grains -- in which case there would be no voids or gaps between the columns, similar to what was described by Messier et al. in reference 22.

Corrosion Resistance of Thin-Film Alloys

Sputter Deposited Alloys

Two or more anodic polarization scans were generated on each of the sputtered thin-films to assess each alloy's corrosion resistance in a 0.1 M chloride environment. The most representative curve, based on visual and optical examination of the specimen before and after testing, was chosen for use in the figures presented in this report.

A comparison of the best anodic polarization behavior for the constant solute concentration Al-W alloys is presented in Figure 25. This figure indicates that the Al120-W alloys (alloys deposited with a power setting of 120 W on the Al target) were more corrosion resistant than the Al240-W alloys (alloys deposited with a power setting of 240 W on the Al target). Breakdown (pitting) potentials for the Al120-6.6%W, Al120-13%W, and Al120-16%W alloys occurred at 320 mV, 452 mV, and 677 mV, respectively; whereas, the Al240-4%W, Al240-6.6%W, Al240-7%W, and Al240-22%W alloys revealed breakdown potentials of -328 mV, -283 mV, 49 mV, and 207 mV,

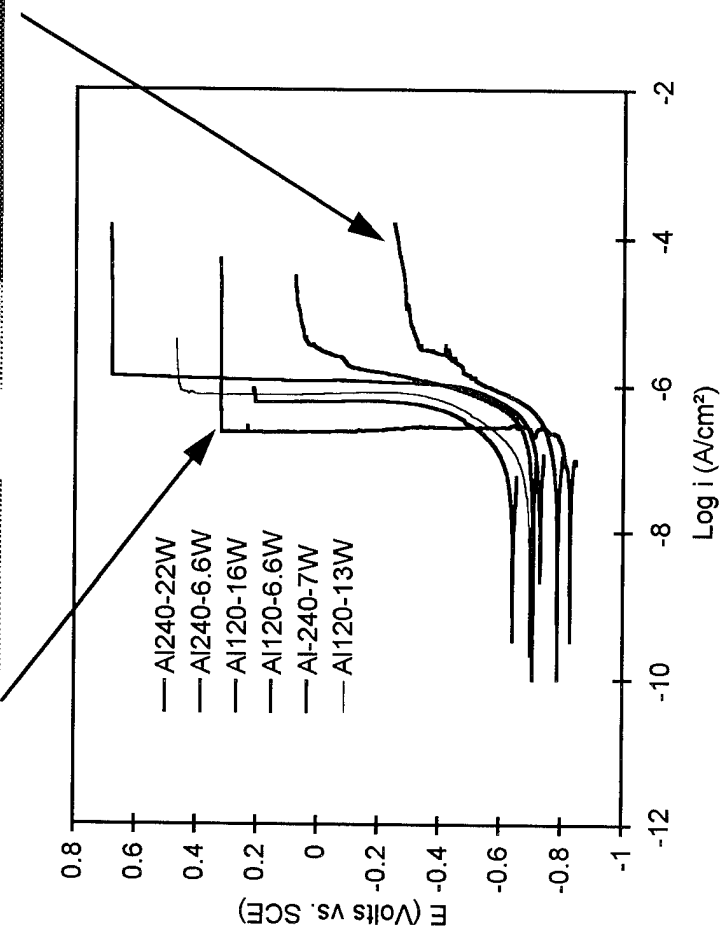
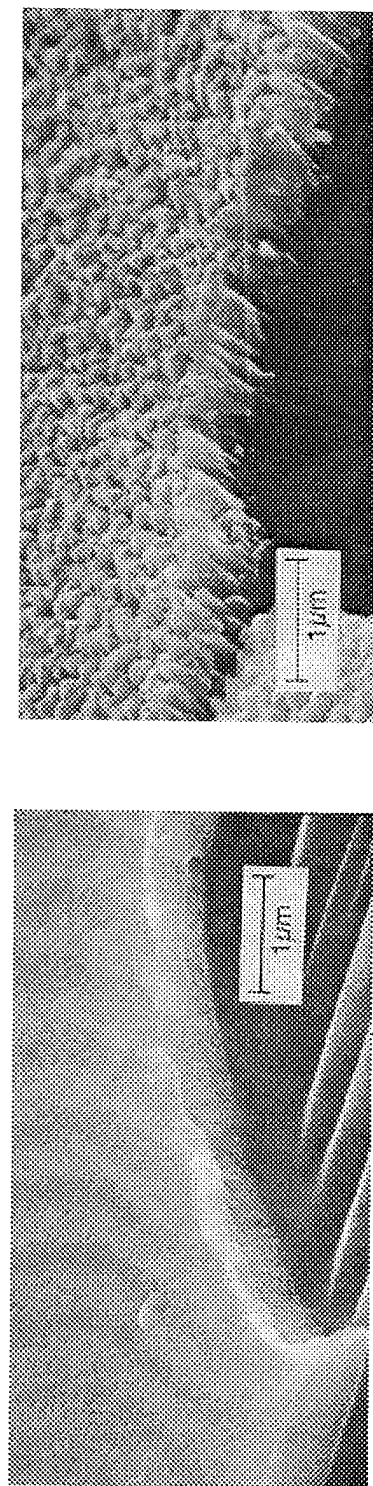


Figure 25. Best anodic polarization curves for selected constant solute Al-W alloys in a 0.1M NaCl solution at a pH of 8 and a scan rate of 0.2 mV/s. This figure illustrates that the improved corrosion resistance of the Al120-W alloys is a result of enhanced film density.

respectively. As Figure 25 reveals, the increased corrosion resistance of the alloys deposited with a power setting of 120 W on the Al target was a result of the smoother and denser morphology of the Al120-W alloys in comparison to the Al240-W alloys. The breakdown potentials for all of the Al-W alloys were significantly higher than that of sputter deposited pure Al, which exhibited a breakdown potential of -719 mV. The corrosion potentials for the Al-W alloys ranged from -838 mV to -641 mV, and were all higher than the corrosion potential for sputter deposited pure Al, which occurred at -1081 mV. The passive current densities for the Al240-7%W and Al240-4%W alloys gradually increased with overpotential, but the other alloys exhibited relatively constant passive current densities in the range of 0.25 to 1 $\mu\text{A}/\text{cm}^2$, which were comparable to the values obtained for the sputter deposited pure Al. Figure 25 shows that in both the Al240-W and Al120-W series, as W concentration increased, both the breakdown potential and corrosion potentials became more noble. The rise in breakdown potential, and in some cases corrosion potential, with increasing W concentration is supported by several studies conducted on Al-W alloys [5-7] and W-containing stainless steels [25,34,35]. Similar improvements in corrosion resistance have also been reported in the literature for Al-Mo alloys [1,2,4] and for Mo-containing stainless steels [36,37].

In comparing the microstructures of the Al240-7%W alloy with those of the Al240-22%W or Al120-6.6%W alloys, a coarse surface with noticeable deep grooves was seen for the Al240-7%W deposit; whereas, the other two deposits appeared relatively smooth. These deep grooves may act as initiation sites for localized corrosion since they essentially represent crevices in the deposit microstructure. Figure 26 illustrates one scenario for establishing localized breakdown of passivity in these creviced regions. This mechanism is very similar to the unified mechanism for crevice corrosion and involves the following steps. Initially, oxygen reduction and metal dissolution occur both outside and inside the groove or crevice. After some time, oxygen depletion at the bottom of the crevice leads to the establishment of an occluded cell with oxygen reduction occurring predominately at the peaks in the deposit and metal dissolution occurring predominately at the bottom of the grooves in the deposit. The pH drops in the grooves as a result of hydrolysis reactions and the chloride ion concentration increases in the grooves in order to maintain electroneutrality. Eventually the passive film breaks down in the grooves as a result of the severe environment. At this stage, propagation of attack in the grooves is driven by oxygen reduction at the peaks. Since the columnar structure of the deposit essentially sets up extremely deep and narrow grooves (or crevices) within the deposit, initiation of localized breakdown of passivity by an IR-induced mechanism is also a distinct possibility. Irrespective of the exact mechanism for the initiation of breakdown, the deep grooves within the deposit will reduce the corrosion resistance of the alloy. Results of this research are supported by those obtained by Thakoor et al. [29] who studied the influence of zone 1 and zone T film microstructures on a material's corrosion performance. Thakoor et al. found that zone T materials, or materials with extremely smooth surfaces and almost featureless cross-sections, were extremely corrosion resistant; whereas, the zone 1 films, which exhibited rougher surfaces, performed significantly worse.

The difference in film thickness between the Al120-W and Al240-W alloys may explain why the thicker Al240-22%W alloy, which appeared to have a smooth surface and a

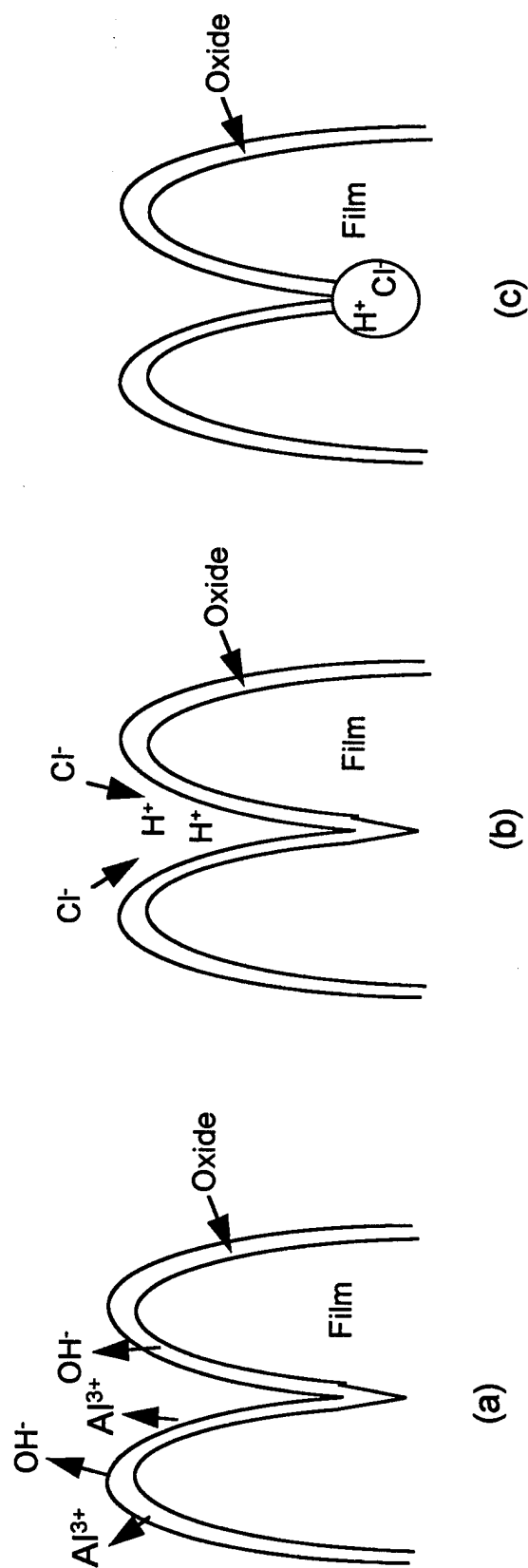


Figure 26. A schematic illustration of a possible mechanism through which localized corrosion could initiate in sputter-deposited, thin-film alloys: (a) Initially oxygen reduction and metal dissolution occur both outside and inside the groove or crevice. (b) An occluded cell is established with time where oxygen reduction occurs mainly at the peaks and metal dissolution occurs predominately in the valleys. (c) Hydrolysis reactions lower the pH of the solution in the valleys, and Cl^- migrates into the valleys in order to maintain electroneutrality. (d) Eventually the passive film permanently breaks down in the valleys and the metal underneath corrodes.

zone 1 microstructure, still performed slightly worse than the thinner Al120-W alloys, including the zone 1 Al120-6%W alloy which had a rough surface. Several researchers [18-22] have shown more and larger features in the physical microstructure of thick deposits. These features, in turn, increase the void network in the thicker deposits leading to decreased corrosion resistance.

The results presented in the last several paragraphs indicate that deposit microstructure plays an extremely important role in determining a film's corrosion resistance. In this regard, the development of alloys with optimal corrosion resistance will require dense alloys with smooth surfaces.

Since the Al120-W alloys outperformed the Al240-W alloys in the anodic polarization experiments, residual stress does not appear to be a primary factor in determining the corrosion resistance of these alloys. Recall that significantly higher tensile residual stresses were recorded for the Al120-W alloys than for the Al240-W alloys. However, exceptionally high residual stresses can cause film buckling or cracking, which will catastrophically diminish the film's corrosion resistance. Note that stress corrosion cracking, which was not evaluated in this study, may be highly dependent on the residual stress of the alloy.

Electron Beam Physical Vapor Deposited Alloys

Not surprisingly, anodic potentiodynamic polarization data for the defective vapor deposited alloys, such as the ones shown in Figures 18 and 19, revealed lower breakdown potentials when compared to their sputter deposited counterparts. Figure 27 compares representative anodic polarization curves for a sputter deposited Al-2.8%Ta alloy and a vapor deposited Al-2.4%Ta alloy. The 200 mV difference in the breakdown potential was attributed primarily to the deep crevices contained in the vapor deposited alloys.

Although a comparison of the anodic polarization data for the sputter and vapor deposited Al-Mo alloys with identical solute concentrations was not possible, Figure 28 reveals that the breakdown potential for a sputter-deposited Al-Mo alloy with an intermediate Mo concentration (10.5 atomic %) was similar to that obtained for a vapor-deposited Al-Mo alloy with an intermediate Mo concentration (11 volume %); however, the passive current density for the e-beam evaporated alloy was approximately 1 order of magnitude higher than that of the sputtered alloy. The e-beam evaporated Al-11v/o Mo alloys in 0.1 M NaCl solution revealed that the open circuit potentials of the vapor deposited alloys were 50 to 100 mV more positive than that of wrought 6061 Al. The 6061 aluminum did not exhibit a passive region in this electrolyte, whereas, the EBPVD alloys exhibited a passive range of approximately 600 mV. Figure 29 reveals that EBPVD specimens containing precipitates exhibited open circuit potentials approximately 100 mV lower than specimens in which all the Mo was in solid solution with the Al. As was also noted in Figure 28, the passive current densities for the precipitate-containing alloys were approximately an order of magnitude higher than those of the solid solution alloys. It should be noted that essentially all of the vapor deposited Al-Mo alloys contained pin hole type defects. Inspection of these pin holes after polarization did not reveal degradation at these sites. This result is likely due to the fact that the pin holes had relatively large

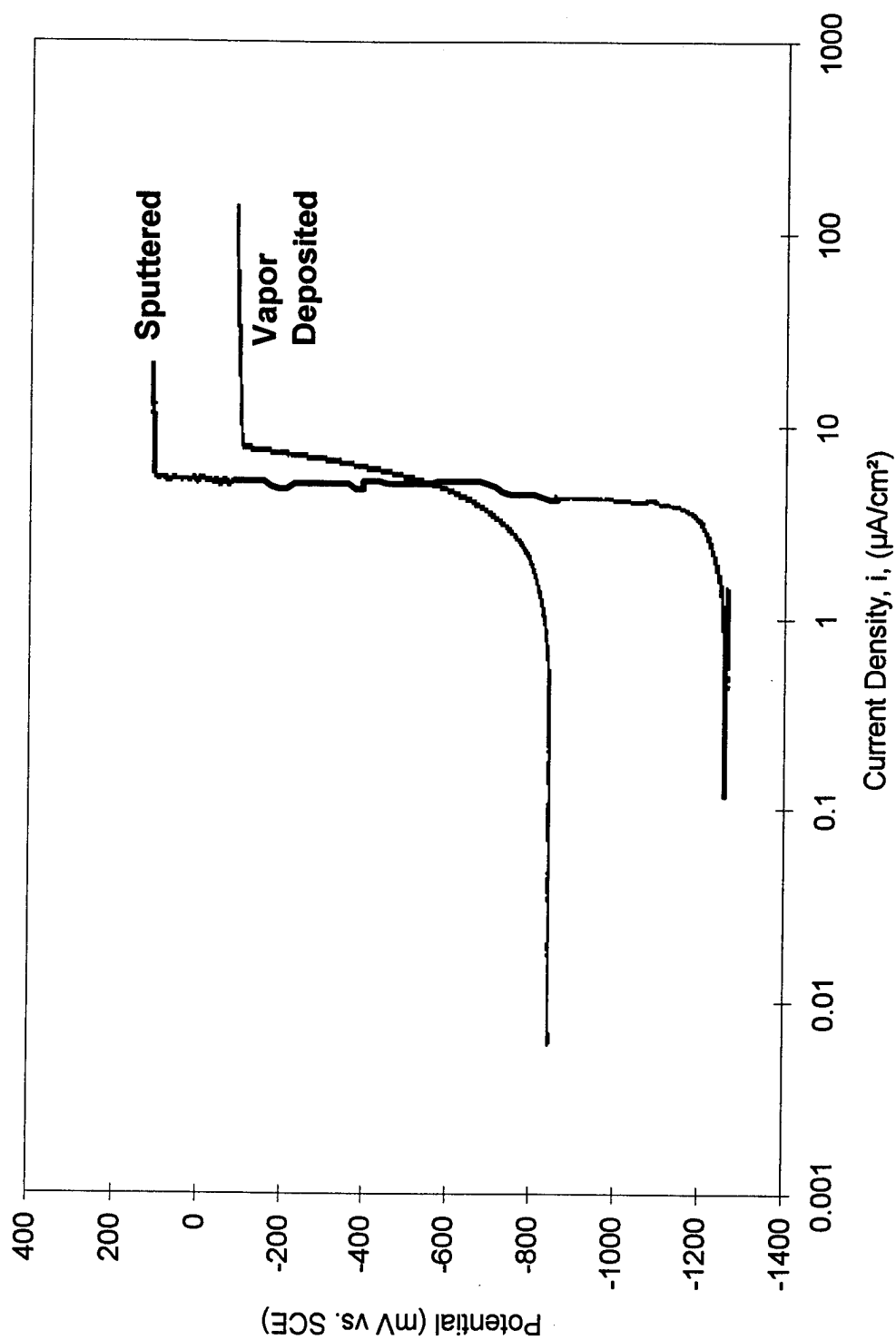


Figure 27. Anodic potentiodynamic scans comparing a sputter deposited Al-2.8%Ta alloy and an EBPVD Al-2.4%Ta alloy polarized in 0.1 M NaCl solution at pH 8.

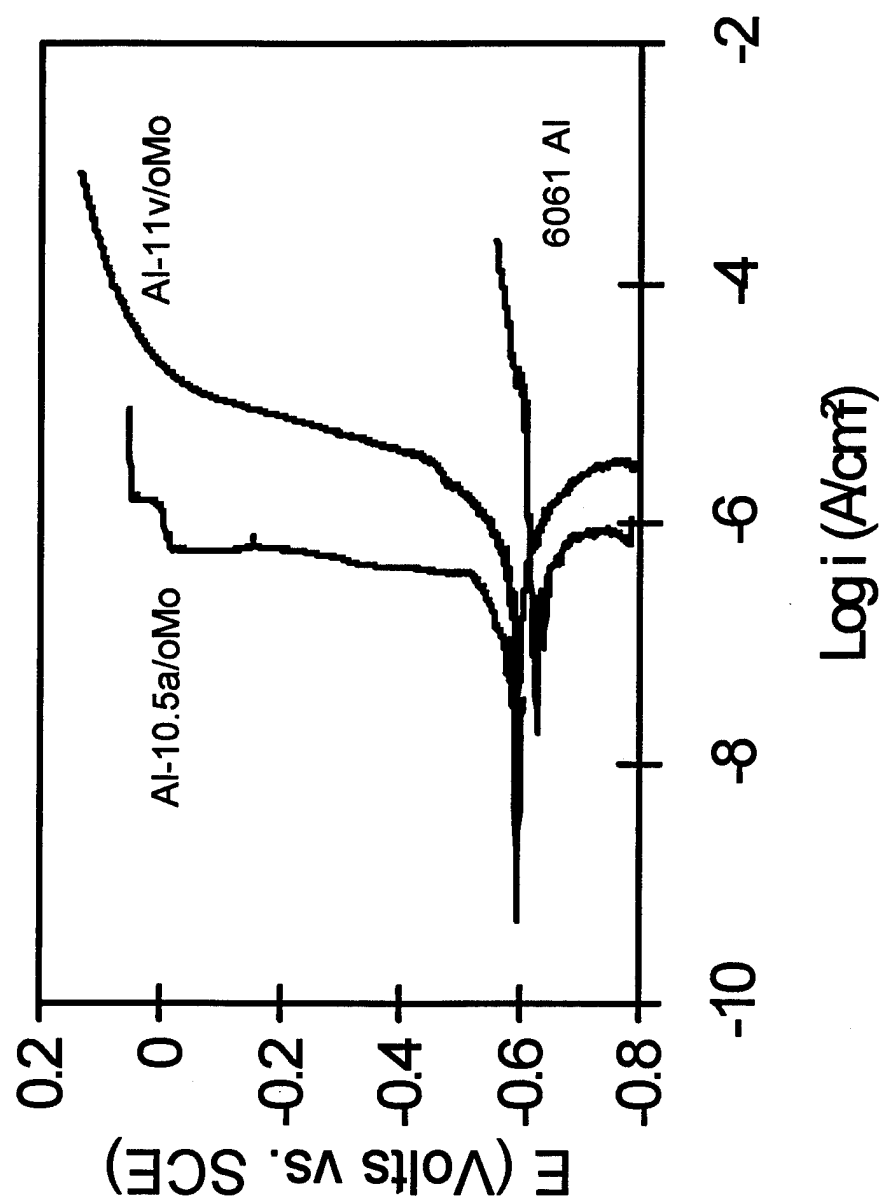


Figure 28. Anodic potentiodynamic scans for sputter deposited Al-10.5a/oMo, 6061Al and an EB-PVD Al-11v/oMo alloy in 0.1 M NaCl solution at pH 8.

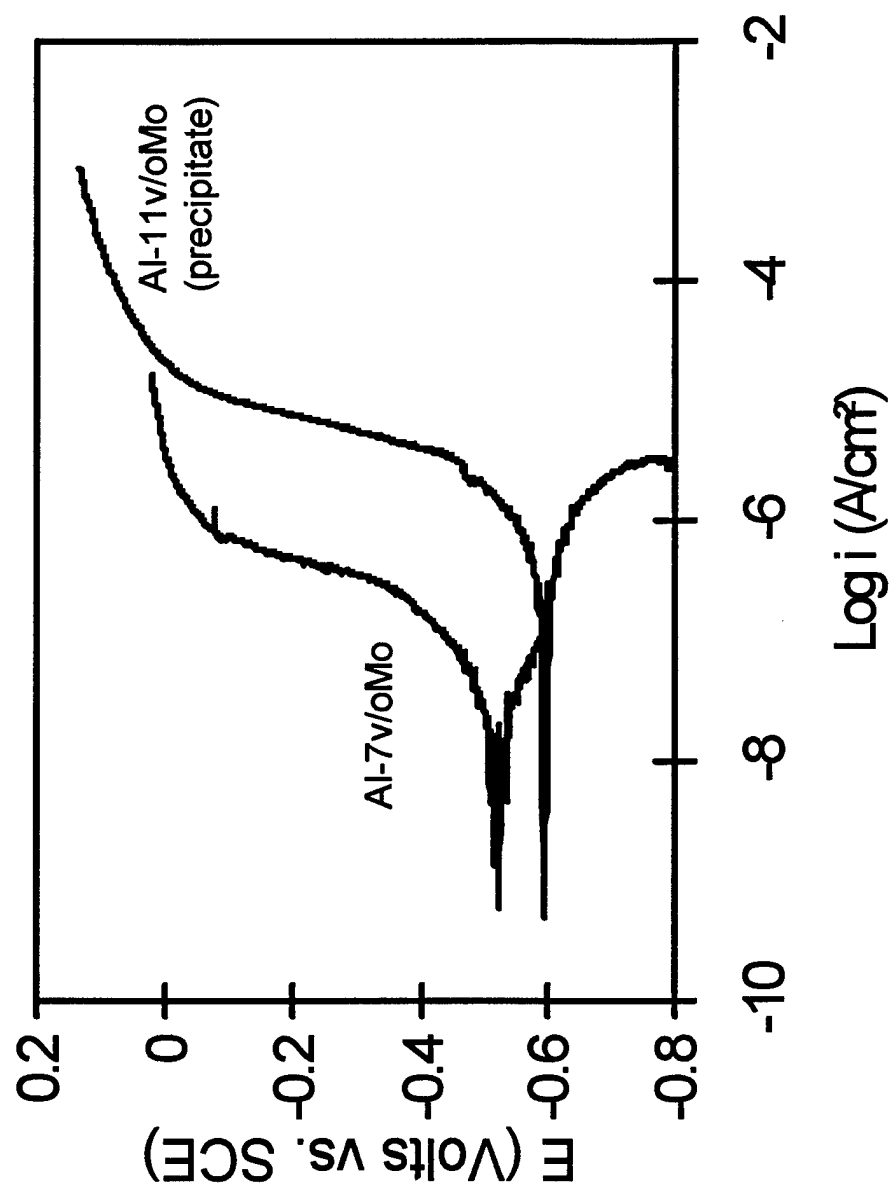


Figure 29. Anodic potentiodynamic scans of EB-PVD Al-Mo alloys with and without precipitates in 0.1 M NaCl solution at pH 8.

diameters.

Compositionally Graded Alloys

In evaluating the corrosion performance of sputter-deposited compositionally graded alloys, the alloys were compared to pure Al and to constant solute alloys that had solute concentrations similar to that of the graded alloy's exposed surface. Results indicated that the graded solute alloys performed slightly worse than the corresponding constant solute alloys. However, all of the alloys performed significantly better than sputter deposited pure Al. Also, the corrosion potentials became more noble with solute additions and were similar in value for both constant and graded alloys. Additionally, the Al-W alloys revealed that alloys with larger compositional gradients performed slightly worse than alloys with shallower compositional gradients.

Figures 30-32 illustrate the anodic polarization behavior for constant and graded alloys with 16, 18 and 32 at/o W, respectively, at their exposed surfaces. These figures revealed that the corrosion potential of the graded and constant solute alloys were similar in value and that these potentials were significantly higher than that of pure Al. Breakdown potentials ranged from 375 mV to 1125 mV for the Al120-32%W series, from 155 mV to 530 mV for the Al120-18%W series, and from 10 mV to 434 mV for the Al120-16%W series alloys with the alloys exhibiting the largest compositional gradients having the lowest breakdown potentials and the constant solute concentration alloys having the highest breakdown potentials. Additionally, the trends in the corrosion and breakdown potentials in the constant solute alloys agreed well with other studies, where both potentials increased with increasing W concentrations. The passive current densities in the Al120-32%W and Al120-18%W series alloys were similar in value for both the constant and graded alloys and were determined to be approximately $0.85 \mu\text{A}/\text{cm}^2$ and $0.664 \mu\text{A}/\text{cm}^2$, respectively. More spread in the passive current densities was noted for the Al120-16%W series alloys with values ranging from approximately $0.60 \mu\text{A}/\text{cm}^2$ to $2.15 \mu\text{A}/\text{cm}^2$ [excluding the graded Al120-(0 to 16)%W alloy]. The passive current density of the Al120-(0 to 16)%W alloy appeared to be dependent on overpotential.

Figure 33 compares anodic polarization behavior of constant and graded solute alloys having 10.5 at/o Mo at the exposed film surface. This figure revealed similar corrosion potentials for the graded and constant solute alloys. The breakdown potential for the constant solute Al-10.5% Mo alloy was 50 mV; whereas, the graded solute Al-(5 to 10.5)%Mo and Al-(9.5 to 10.5)%Mo alloys showed breakdown potentials of -40 mV and -20 mV, respectively. Thus, the breakdown potentials for the graded alloys were approximately 70 to 90 mV lower than the values observed for the Al-10.5% Mo constant solute alloy. However, the breakdown potentials for all of the graded alloys were still significantly higher than the breakdown potential of sputter deposited pure Al. The passive current densities for the Al-10.5% Mo alloy and the graded Al-(5 to 10.5)%Mo alloy were $0.562 \mu\text{A}/\text{cm}^2$ and $1.26 \mu\text{A}/\text{cm}^2$, respectively. The graded Al-(9.5 to 10.5)%Mo alloy showed a passive current density that continuously increased with potential until a potential of -250 mV was reached. At potentials greater than -250 mV,

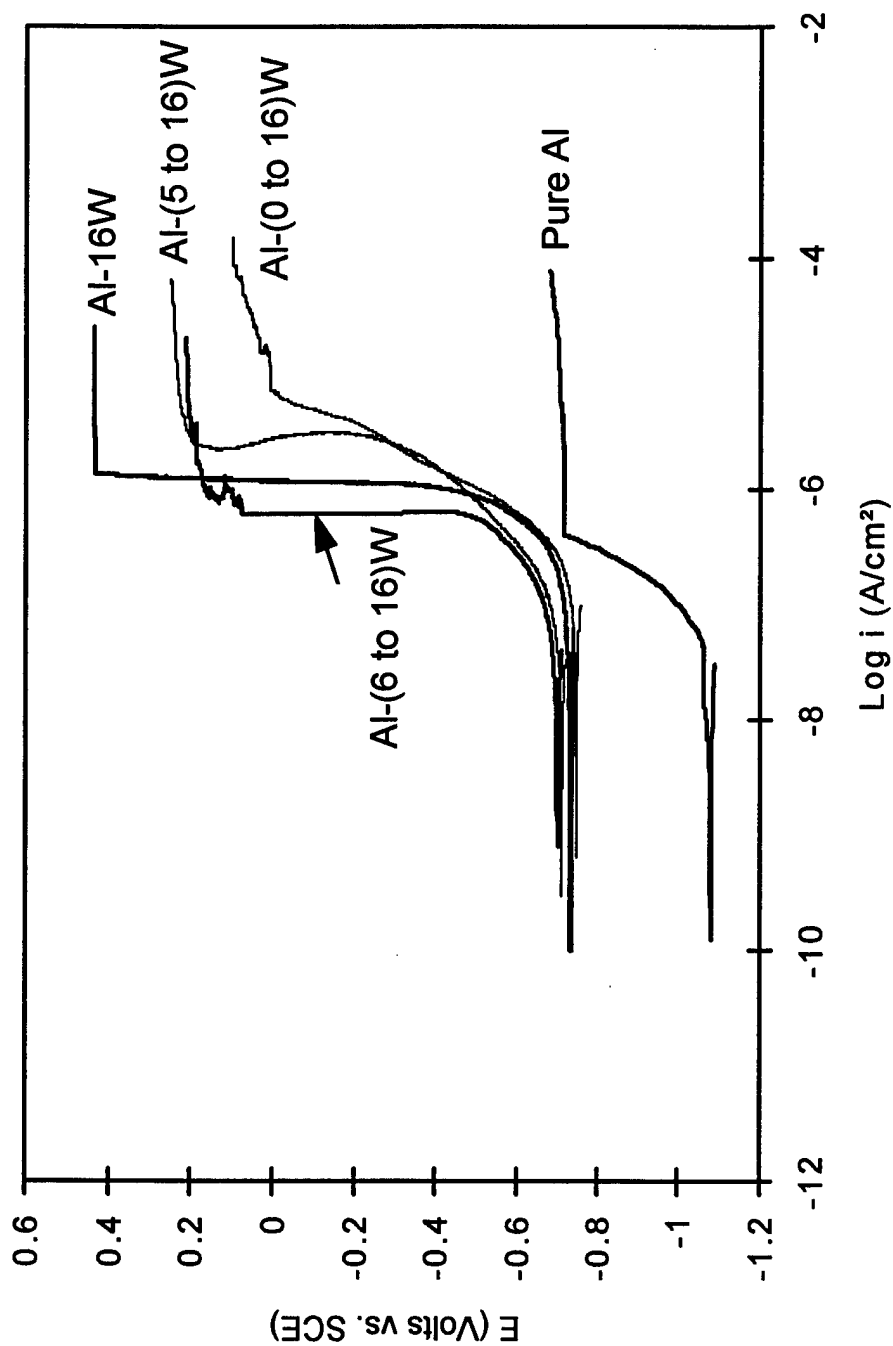


Figure 30. A comparison of anodic polarization curves for constant and graded alloys having 16 a/oW at the exposed outer layer of the deposit. Tests were conducted in 0.1M NaCl solution at a pH of 8 and a scan rate of 0.2 mV/s. (Alloys produced at PSU-MRL)

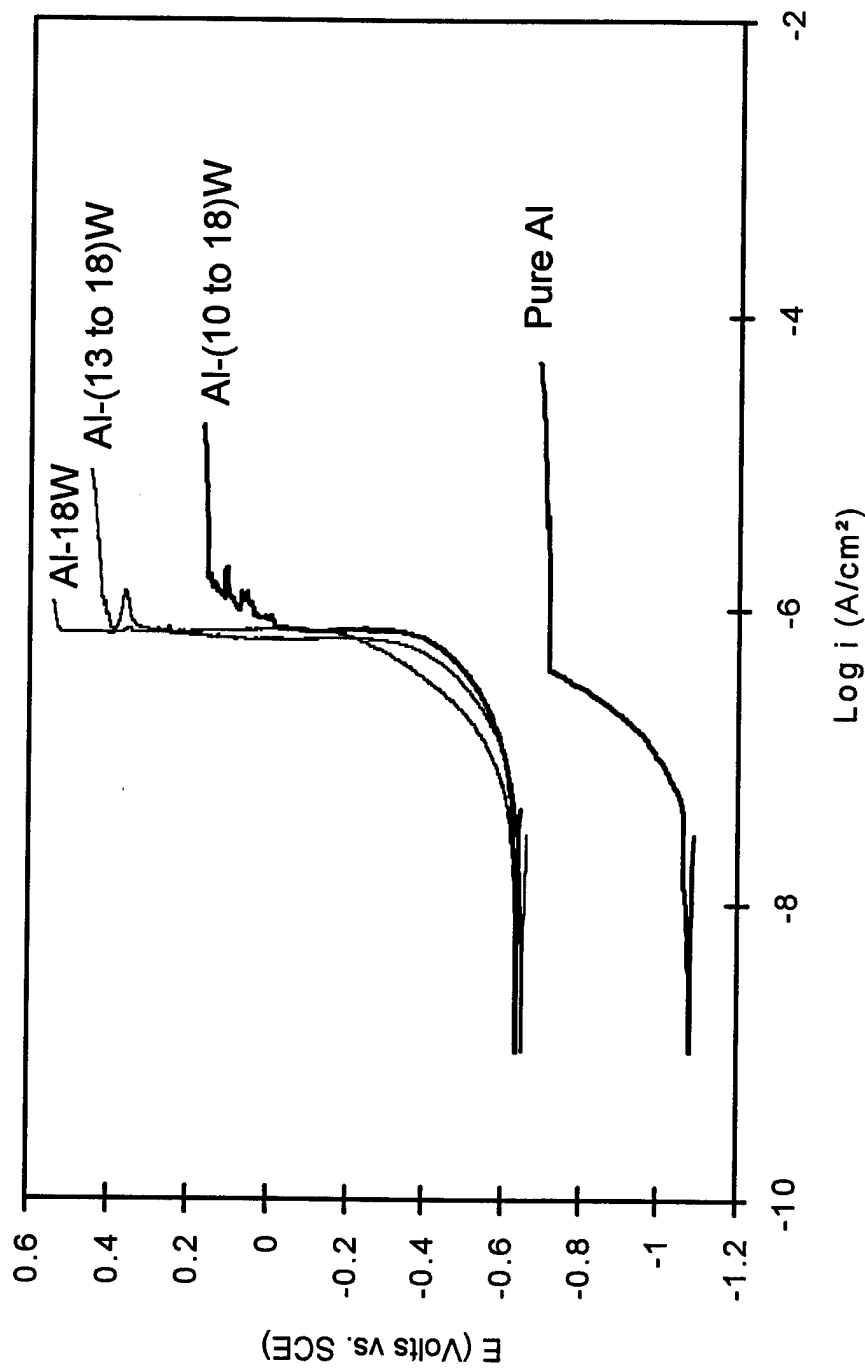


Figure 31. A comparison of anodic polarization curves for constant and graded alloys having 18 a/oW at the exposed outer layer of the deposit. Tests were conducted in 0.1M NaCl solution at a pH of 8 and a scan rate of 0.2 mV/s. (Alloys produced at PSU-MRL)

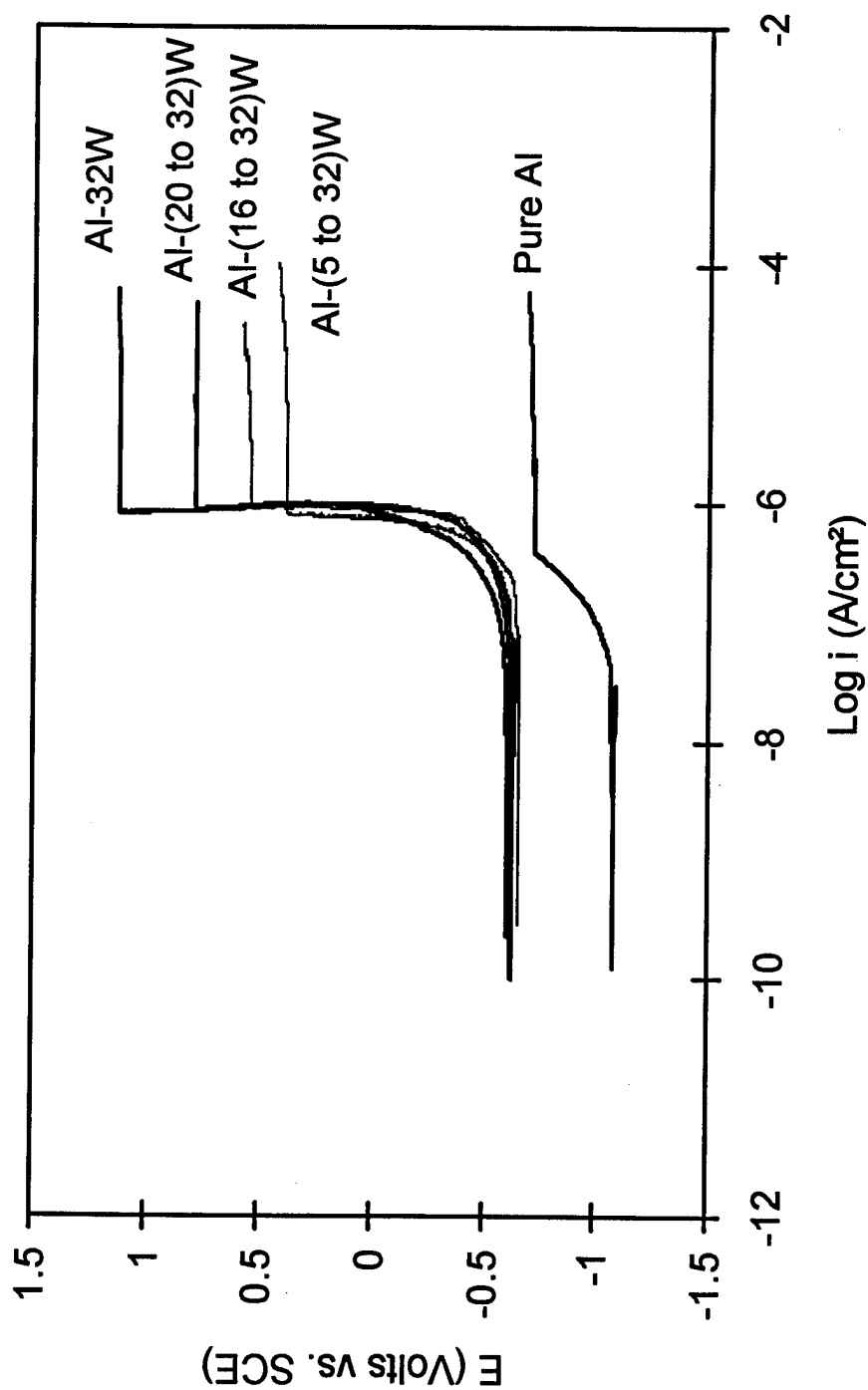


Figure 32. A comparison of anodic polarization curves for constant and graded alloys having 32 a/oW at the exposed outer layer of the deposit. Tests were conducted in 0.1M NaCl solution at a pH of 8 and a scan rate of 0.2 mV/s. (Alloys produced at PSU-MRL)

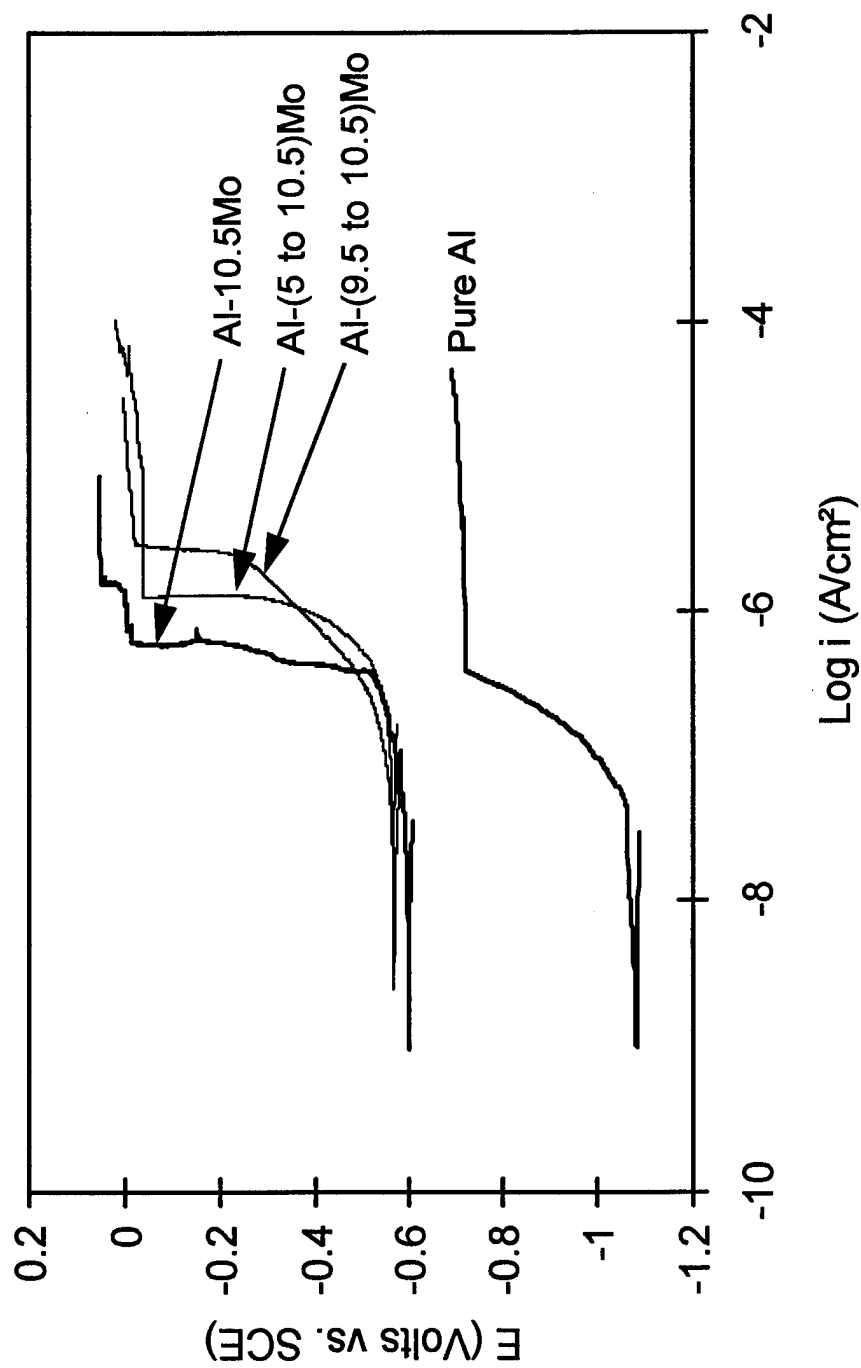


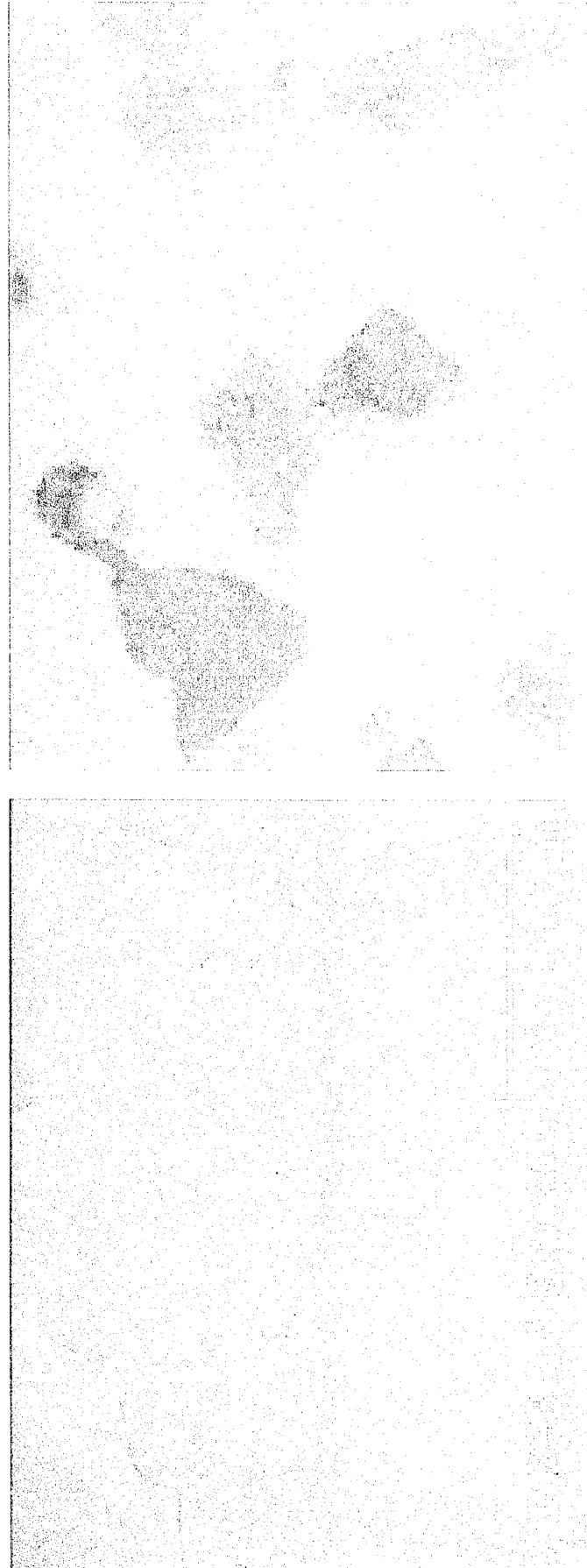
Figure 33. A comparison of anodic polarization curves for constant and graded alloys having 10.5 a/oW at the exposed outer layer of the deposit. Tests were conducted in 0.1M NaCl solution at a pH of 8 and a scan rate of 0.2 mV/s. (Alloys produced at PSU-MRL)

the passive current density for this alloy remained constant at $2.51 \mu\text{A}/\text{cm}^2$. Note that the passive current density for the constant solute Al-10.5%-Mo alloy compared well with that of sputter deposited pure Al; whereas, the passive current densities for the graded alloys appeared to be slightly higher than that of pure Al. An Auger image of one of the Al-Mo alloys after polarization, see Figure 34, revealed that breakdown (pitting) sites were depleted of Al and enriched in the solute. This observation of dramatic solute enrichment within pits is consistent with the solute-rich interphase mechanism which was proposed earlier by Shaw and Davis to explain the exceptional pitting corrosion resistance of thin-film nonequilibrium Al alloys [6,7].

The anodic polarization results for the graded alloys indicated that these alloys performed slightly worse than the constant solute alloys. Additionally, alloys with large compositional gradients performed worse than those with small compositional gradients. One possible explanation for this behavior may stem from defects such as the ones shown in Figures 9-13. These defects can expose underlying layers with lower solute concentrations which lowers the corrosion resistance of the thin-film alloy since their corrosion resistance typically improves with increasing solute concentration. Furthermore, a graded alloy exhibiting a zone 2 or zone 1 microstructure at its surface may also expose regions of lower solute concentration at the bottom of grooves or crevices in the deposit, significantly reducing the corrosion resistance of the deposit. For example, the Al-(<0.5 to 5)%Mo alloy in Figure 17 b contained deep surface grooves. These deep grooves in the microstructure could expose layers of lower solute concentration, as depicted in Figure 35. As this schematic illustrates, the base of the grooves may expose low solute concentration regions which are less corrosion resistant than the alloy present at the column tops. It should be noted that the corrosion potential of the Al-(>0.5 to 5)Mo alloy was higher than that of pure Al and slightly less than that of Al-5% Mo, but the passive range was small and breakdown occurred at a very low potential. An evaluation of the Al-32%W series alloys indicated that alloys with larger compositional gradients performed worse than alloys with smaller compositional gradients. In this case, the surfaces of the alloys were smoother than the zone 2 Al-(0.5 to 5) alloys, but they still showed some topographical features (consisting of small "hills" separated by shallow "valleys", similar to that of a zone 1 microstructure). Also, columnar growth was still present in the Al-32%W series alloy cross-sections. The low points or crevices on the film surface, (exposed by the columnar growth and surface features) may contain regions of lower solute concentration than the top layer or high points in the deposit. Therefore, columnar deposits with large compositional gradients will likely expose regions of very low solute concentration at the base of the columnar structure and exhibit lower corrosion resistance than columnar deposits with smaller compositional gradients.

Fabrication of PSU Vapor Deposition System

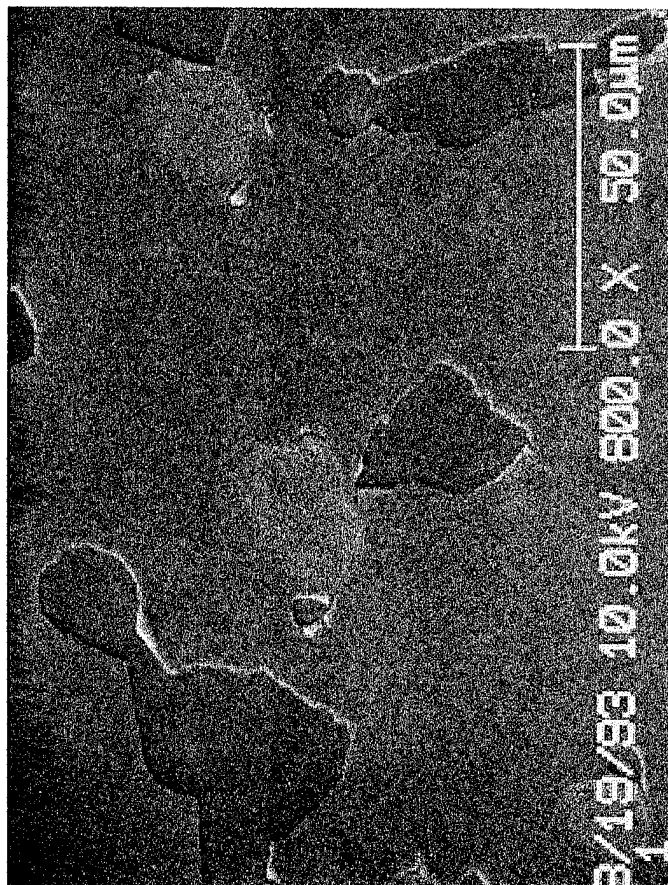
During the past year, fabrication of an e-beam physical vapor deposition system was initiated at Penn State. A schematic illustration of the dual target system is presented in Figure 36. At the present time, the final stages of the system fabrication are being completed.



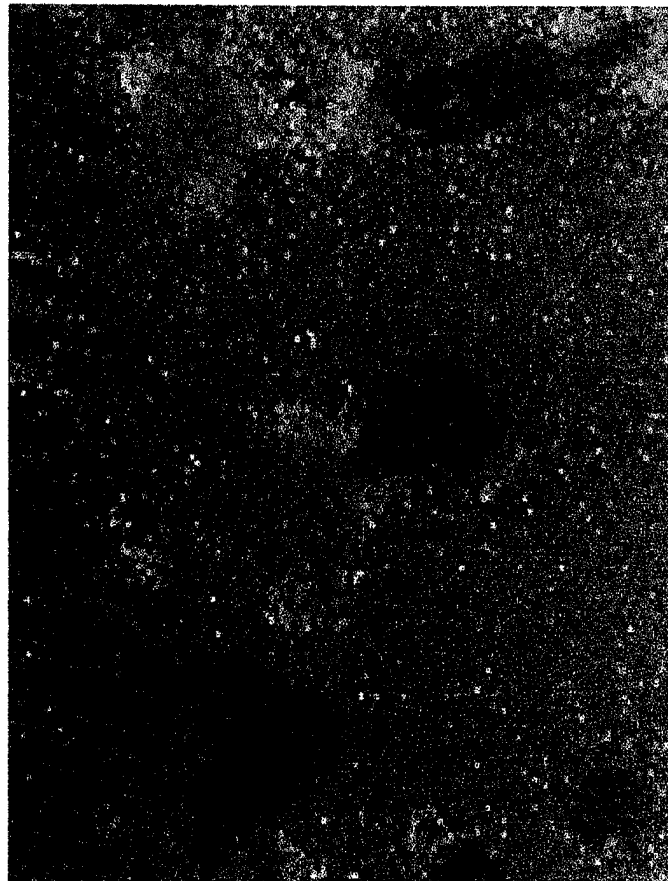
(a)

(b)

Figure 34. (a) a SEM image of Al-9Mo film showing areas of attack after polarization, and (b) corresponding Auger image showing enrichment of molybdenum at the areas of attack (red), while the green area represents aluminum and the blue area represents the silicon substrate.



(a)



(b)

Figure 34. (a) a SEM image of Al-9Mo film showing areas of attack after polarization, and (b) corresponding Auger image showing enrichment of molybdenum at the areas of attack (red), while the green area represents aluminum and the blue area represents the silicon substrate.

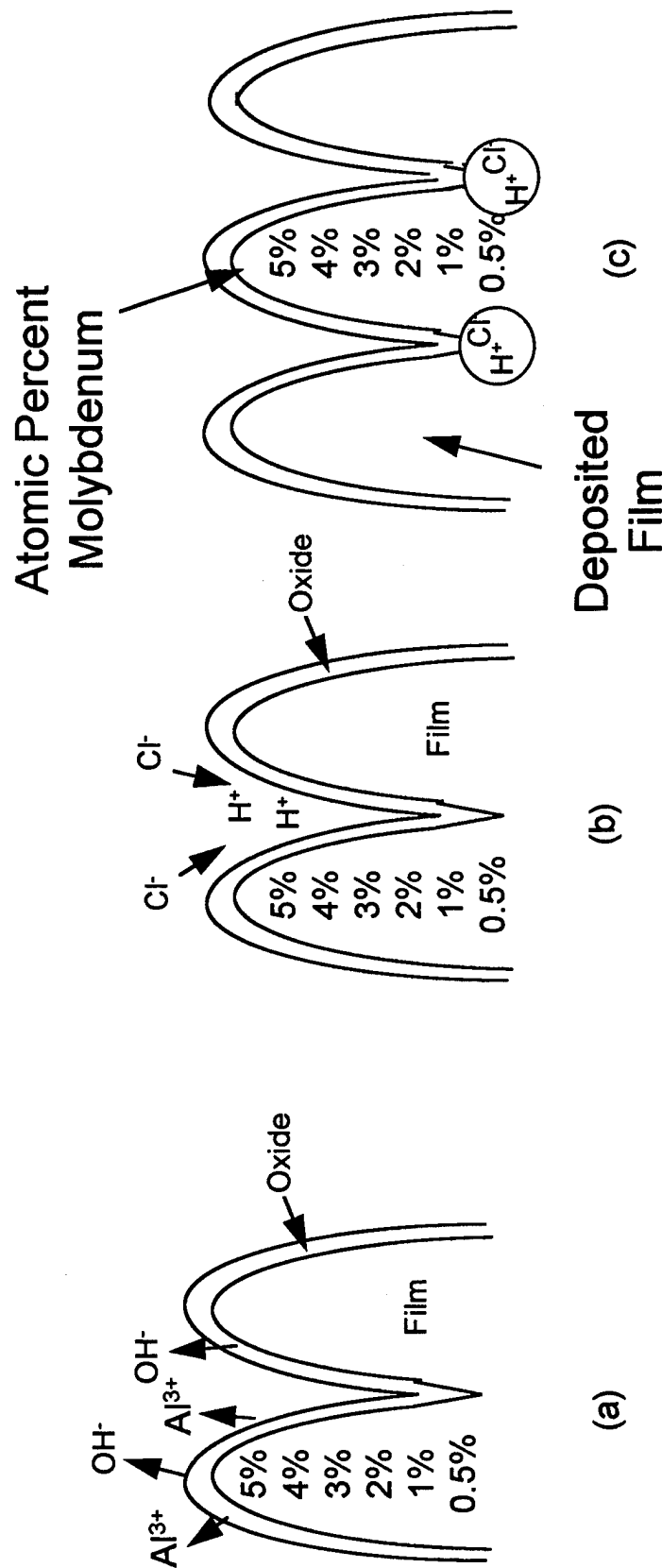


Figure 35. Schematic illustration of a three step process which could lead to pitting of thin-film graded alloys which have an exceedingly columnar structure by attacking the areas where the solute concentration is least. The steps in this process are identical to the ones presented in Figure 27; however, in this case the grooves (or valleys) in the deposit are the regions in which the solute concentration, or corrosion resistance, is the lowest.

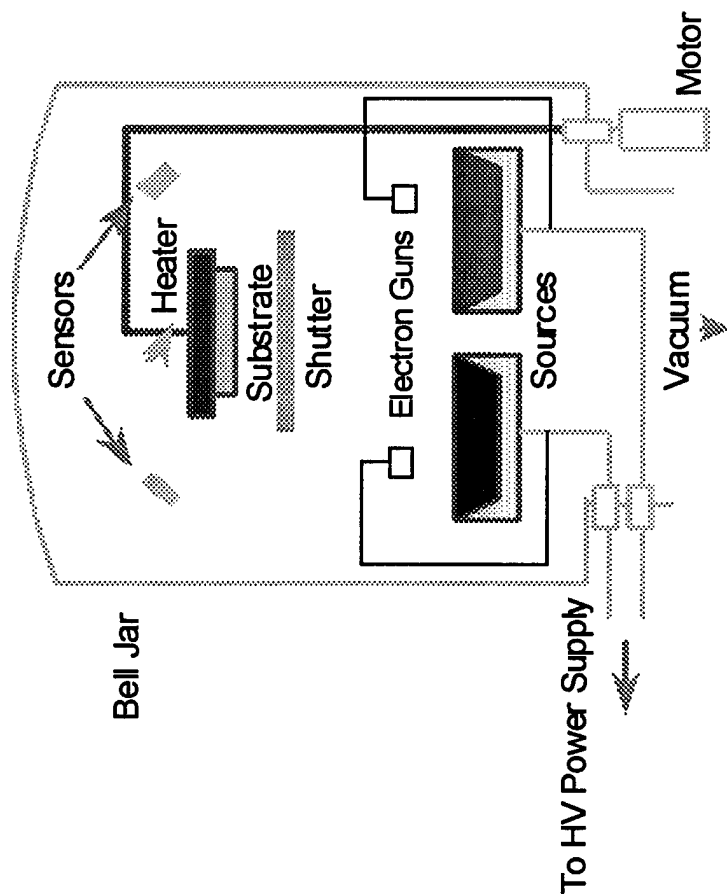


Figure 36. Schematic illustration of PSU dual source EBPVD system.

SUMMARY

Results obtained within the last year have shown that it is possible to produce e-beam evaporated Al-Mo Alloys which have significantly enhanced localized corrosion resistance. For example, an Al -7 volume percent Mo alloy exhibited a breakdown (pitting) potential that was 600 mV higher than that of 6061 Al. As a result of the higher deposition temperatures for the e-beam evaporation process, precipitates were noted in the e-beam evaporated alloys when deposition temperatures were in excess of 300 C. Fortunately, the presence of these precipitates did not severely alter the range of passivity for the alloys (as measured in an anodic polarization scan); instead, the precipitates increased the passive current densities of the alloys by about an order of magnitude. Preliminary cross-sectional analysis of the e-beam evaporated materials revealed that the initial 25 to 50 % of the deposit (5 to 10 microns) was very dense, whereas, the top 50 to 75 % of the deposit was very columnar in structure with open regions between the columns. This columnar part of the deposit is not attractive from a corrosion standpoint and work in the coming year will focus on producing deposits without columnar structures.

Research on both the sputter and e-beam evaporated materials has clearly shown that defects and deposit morphology (e.g., a columnar structure) play a significant role in pit initiation (breakdown) on these materials. Morphological changes were apparent in the compositionally graded sputter-deposited materials and the degraded performance of these alloys, when compared to the constant solute concentration alloys, was attributed to pit initiation in low solute concentration regions of the deposit (regions at the bottom of deep grooves in the columnar structure). Clearly, full optimization of deposit corrosion resistance will hinge on the production of smooth, dense deposits which do not exhibit a columnar structure. The superior corrosion resistance of the nonequilibrium sputter and e-beam evaporated alloys, despite their less than optimal morphologies, is believed to be the result of enhanced repassivation of the alloys caused by solute enrichment at pit initiation sites.

References

1. W.C. Moshier, G.D. Davis, J.S. Ahearn, and H.F. Hough, J. Electrochem. Soc., 133, 1063 (1986).
2. W.C. Moshier, G.D. Davis, J.S. Ahearn, and H.F. Hough, J. Electrochem. Soc., 134, 2677 (1987).
3. W.C. Moshier, G.D. Davis, and G.O. Cote, J. Electrochem Soc., 136, 356 (1989).
4. G.D. Davis, W.C. Moshier, T.L. Fritz and G.O. Cote, J. Electrochem. Soc., 137, 422 (1990).
5. B.A. Shaw, T.L. Fritz, G.D. Davis, and W.C. Mosher, J. Electrochem. Soc., 137, 1317 (1990).
6. B.A. Shaw, G.D. Davis, T.L. Fritz, B.J. Rees and W.C. Mosher, J. Electrochem. Soc., 138, 3288 (1991).

7. G.D. Davis, B.A. Shaw, B.J. Rees and M. Ferry, *J. Electrochem. Soc.*, 140, 951 (1993).
8. T.R. Schrecengost, B.A. Shaw, R.G. Wendt and W.C. Moshier, *Corrosion*, 49, 842 (1993).
9. R.G. Wendt, W.C. Moshier, B.A. Shaw and P.L. Miller, *Corrosion*, 50, 820 (1994).
10. G.D. Davis, B.A. Shaw, B.J. Rees and C.A. Pecile, *Surface and Interface Analysis*, 22, 609 (1995).
11. P.G. Partridge and M.C. McConnel, *Acta Metall.*, 35, 1973 (1987).
12. P.G. Partridge and M.C. McConnel, *Acta Metall.*, 35, 1981 (1987).
13. R.L. Bickerdike, D. Clark, J.N. Eastabrook, G. Hughes, W.N. Mair, P.G. Partridge and H.C. Ranson, *International Journal of Rapid Solidification*, 2, 1 (1986).
14. F.H. Froes, C. Suryanarayana, K.C. Russell and C.M. Ward-Close, *Proc. Int. Conf. on Novel Techniques in Synthesis and Processing of Advanced Materials*, eds. J. Singh and S.M. Copley (1994).
15. M. Fass, D. Itzhak, D. Eliezer and F. H. Froes, *J. Mater. Sci. Lett.*, 6, 1227 (1987).
16. B.A. Movchan, A.V. Demchishin, *Fiz. Met. Metalloved*, 28, 653 (1969).
17. J.A. Thornton and D.W. Hoffman, *Thin Solid Films*, 171, 5 (1989).
18. R. Messier, A.P. Giri and R.A. Roy, *J. Vac. Sci. Technol. A.*, 2(2) 500 (1984).
19. R.A. Roy and R. Messier, *J. Vac. Sci. Technol. A.*, 2(2) 312 (1984).
20. R. Messier, *J. Vac. Sci. Technol. A*, 4(3), 490 (1986).
21. Private discussions with Dr. Russell Messier.
22. R. Messier and R.C. Ross, *J. Appl. Phys.*, 53(9), 6220 (1982).
23. P. Chaudhari, *J. Appl. Phys.*, 45(10), 4339 (1974).
24. G.J. van der Kolk, M.J. Verkerk and W.A.M.C. Brankaert, *Semiconductor International*, 11, 224 (1988).
25. N. Bui, A. Ihrzgo, F. Dabosi and Y. Limouzin-Maire, *Corrosion*, 39(12), 491 (1983).
26. A.G. Dirks, J.J. van den Broek and P.E. Wierenga, *J. Appl. Phys.*, 55(12), 4248 (1984).
27. P. Miller, *Corrosion Characteristics of Nonequilibrium Magnesium-Yttrium Alloys*, Masters Thesis, The Pennsylvania State University (1994).

28. B.A. Shaw and K.A. Kennedy, *Enhancement of Corrosion Resistance and Mechanical Properties of Light-Weight Metals Through the Use of Graded Nonequilibrium Microstructures*, ONR Report (1994).
29. A.P. Thakoor, S.K. Khanna, R.M. Williams and R.F. Landel, J. Vac. Sci. Technol. A, 1(2), 520 (1983).
30. G.D. Davis, W.C. Moshier, G.G. Long, and D.R. Black, J. Electrochem. Soc., 138(11), 3194 (1991).
31. P.L. Miller, B.A. Shaw, R.G. Wendt and W.C. Moshier, Corrosion, 49, 947 (1993).
32. P.L. Miller, B.A. Shaw, R.G. Wendt and W.C. Moshier, Corrosion, 51, 922 (1995).
33. K.A. Kennedy, *The Influence of Film Morphology and Residual Stress on the Corrosion Resistance of Co-Sputter Deposited, Compositionally Graded and Constant Solute Aluminum Thin Films*, Masters Thesis, The Pennsylvania State University (1995).
34. A. Irhzo, Y. Segul, N. Bui and F. Dabosi, Corrosion Science, 26(10), 769 (1986).
35. A. Irhzo, M. El, Saffy, N. Bui and F. Dabosi, Key Engineering Mater., 20-28(4), 3953.
36. K. Sugimoto and Y. Sawada, Corrosion Science, 17, 425 (1977).
37. J.B. Lumsden, Passivity of Metals, eds. R.P. Frankenthal and J. Kruger, 730 (1978).